Integrated Optimization of Thermoelectric Systems

by

Aaron Paul Schlenker

B.S., United States Military Academy (2018)

Submitted to the Department of Mechanical Engineering
in partial fulfillment of the requirements for the degree of

Master of Science in Mechanical Engineering

at the

MASSACHUSETTS INSTITUTE OF TECHNOLOGY

May 2020

Author .....
Department of Mechanical Engineering
May 15, 2020

Certified by .....
Asegun S. Henry
Robert N. Noyce Career Development Professor
Thesis Supervisor

Certified by .....
Kasey J. Russell
Principal Member of the Technical Staff, Draper
Thesis Supervisor

Accepted by .....
Nicolas G. Hadjiconstantinou
Chair, Department Committee on Graduate Theses

Integrated Optimization of Thermoelectric Systems

by

Aaron Paul Schlenker

Submitted to the Department of Mechanical Engineering
on May 15, 2020, in partial fulfillment of the
requirements for the degree of
Master of Science in Mechanical Engineering

Abstract

Thermoelectric devices present unique opportunities for sustainable energy conversion. While research efforts have remarkably improved material capabilities over the past several decades, material advancement alone is insufficient to realize the full potential of thermoelectric technology [25, 24, 39, 14]. Here, an integrated perspective is applied to thermoelectric technology to identify potential system improvements. The traditional thermoelectric architecture is dissected to identify limitations. It is found that the coupling of the device height to the thermoelectric element height imposed by the architecture can significantly hinder performance. A novel distributed architecture, which de-couples the device and element heights, is theorized to address these limitations. A modeling program incorporating device parameters and external conditions is developed to simulate and optimize the system architecture. The new architecture is shown to out-perform the traditional architecture in both a broad range of general generation and refrigeration conditions and the specific application of a phase-change material thermoelectric generator. The results signal the importance and potential value of an integrated approach to thermoelectric system design.

Thesis Supervisor: Asegun S. Henry
Title: Robert N. Noyce Career Development Professor

Thesis Supervisor: Kasey J. Russell
Title: Principal Member of the Technical Staff, Draper

Acknowledgments

Funding for this work was provided by The Charles Stark Draper Laboratory, Inc.

I am grateful for the opportunity here to reflect and thank those individuals who have aided me in this endeavor, and more importantly who have helped me grow personally through the process. Though I regret not showing my gratitude more frequently, I hope these words convey how much I appreciate your investment in my life. This could not be more true for my wife, Samantha. Thank you for the small things – making sure I had enough to eat, keeping me on task, and reminding me to shower daily – and for the big things – encouraging me, motivating me, and supporting me through this process. Whether together or apart, your continued sacrifices have made this possible, and I will not soon forget all you have done for me. I love you.

I am also indebted to many outstanding individuals at Draper. To the entire ICE-T team, I greatly enjoyed learning from your work and always left our weekly meetings with new ideas and inspirations. I regret not moving more quickly with my work, as I was looking forward to getting to the point where materials and system design would merge and I would get to interact more closely with you all. I wish you all the best and hope that our paths cross again. To Kasey and Cáit specifically, thank you for your mentorship, guidance, and friendship. Looking back at my time, I can say that I truly enjoyed working on this project, in large part due to your contagious enthusiasm and energy. Kasey, you have been an outstanding supervisor. Thank you for providing direction and advice but leaving room for initiative – I feel that I have well fulfilled the purpose of a Master's program. More importantly, I am grateful for the example you have given me of work-life balance and personal leadership, which I hope I will be able to emulate myself in the future. I would also like to thank Martha and Sheila for coordinating the Draper Fellow program and providing me with this incredible opportunity.

Meaningful friendships have made this experience unforgettable. From weekday ski trips to Saturday college football parties, to nights at Fenway and The Garden, in the gym playing basketball, or just playing cards after dinner, I will leave Cambridge and Boston with many great memories. To Noah, Jack, Helen, Logan, Kristen, Gabe, John, Sam, Connor, Noah D., Jordyn, Wade, Anna, and Brian: thank you for your friendship, and I look forward to seeing you again in the future. I would like to thank Noah Siegel in particular for being a great roommate and friend, who I bonded with easily over our shared love of call options and hatred of bitmapped graphics (readers can search for one if they like but will only find Ti*k*Z graphics).

Finally, thank you to my family, in particular my parents and brother, for your unconditional love and support. This work is directly a result of your many years of selfless investment in my life.

> *He who forms the mountains, who creates the wind, and who reveals his thoughts to mankind, who turns dawn to darkness, and treads on the heights of the earth— the* Lord *God Almighty is his name.*

Contents

List of Figures

List of Tables

This page intentionally left blank.

Nomenclature

Variables

$2d$	element spacing	m
$\dot{W}$	electric power	W
$\mathcal{L}$	latent heat	J
A	total area of n-p pair	m^2
c	$l_{w,mid}/l_{w,tot}$	
E	electric potential	V
g	gap length (Roters)	
h	height (refers to Roters if not subscripted)	m
I	current	A
K	thermal conductance	
k	thermal conductivity	$\frac{\mathrm{W}}{\mathrm{m\,K}}$
l	length (refers to Roters if not subscripted)	m
L_f	latent heat of fusion	$\frac{\mathrm{J}}{\mathrm{kg}}$
M	load resistance ratio	
N	number of pairs	
P	magnetic permeance	H
Q	internal energy	J
q_j	Joule heat flow	W
r	radius of fringing	m
R_e	electrical resistance	Ω
R_t	thermal resistance	$\frac{\mathrm{K}}{\mathrm{W}}$
S	Seebeck coefficient	$\frac{\mathrm{V}}{\mathrm{K}}$
s	compatibility factor	
T	temperature	K
U	overall heat transfer coefficient	$\frac{\mathrm{W}}{\mathrm{m^2\,K}}$
u	I/q_{te}	
w	width (refers to Roters if not subscripted)	m
ZT	figure of merit	
χ	spreading dimension ratio	
η	efficiency	
η_c	Carnot efficiency	
η_r	reduced efficiency	
γ	Peltier heat ratio	
Λ	non-dimensional conductance	
μ	magnetic permeability	$\frac{\mathrm{H}}{\mathrm{m}}$
Φ	non-dimensional fringing	
ϕ	coefficient of performance	
ρ	density	$\frac{\mathrm{kg}}{\mathrm{m^3}}$
σ	electrical conductivity	$\frac{\mathrm{S}}{\mathrm{m}}$

Subscripts

PCM	phase-change material
c	interface contact
fr	thermal fringing
ins	insulation
$load$	attached electrical load
mod	entire module
net	net
o	known or applied value
pl	exterior plate
s	thermal spreading
sim	simulated
snk	external heat sink
src	external heat source
t	thermal
te	thermoelectric pair
tot	total for n-p pair
w	wire

Chapter 1

Introduction

Over the past few decades, an increased focus on renewable energy and the expansion of the semiconductor industry have revived interest in thermoelectric technology [28]. Thermoelectric technology presents an opportunity for waste heat recovery and low-power, solid-state refrigeration, but poor efficiency has hampered broad implementation. Research has therefore largely focused on improving efficiency, primarily through development and enhancement of thermoelectric materials which set the upper limit of energy conversion efficiency [39]. This work has been well summarized [39, 14, 51, 36].

While this extensive materials research has produced promising progress, other research has found that material advancement alone is insufficient to realize the full potential of thermoelectric technology [25, 24, 39, 14]. Another key factor identified in such work is system design and system-level heat transfer. Like all systems, device design and architecture influence performance, and although a few alternative designs have been introduced recently [5, 27], devices have largely been built on one basic, unchanged architecture. Consequently, device performance is often handicapped regardless of material potential.

The purpose of this work is to underscore the importance of an integrated system design approach and introduce a novel architecture that expands the system design space. Chapter 2 introduces fundamental thermoelectric concepts and the traditional architecture. Measures of performance are derived and analyzed to show the limitations and deficiencies of the traditional architecture. Chapter 3 explores a novel

distributed architecture that may remedy these deficiencies. To attain the desired integrated perspective and handle the added complexity of the distributed architecture, modeling software for integrated system simulation and optimization is developed in Chapter 4. Chapter 5 presents general simulated performance and comparisons to traditional architecture. In Chapter 6, the novel architecture is applied to a specific scenario. The final chapter contains some concluding thoughts and identifies areas for continued research.

Chapter 2

Traditional Thermoelectric Design

In this chapter, the traditional thermoelectric system architecture is presented and analyzed. A brief explanation of thermoelectric fundamentals is provided through which the traditional architecture is introduced. The expected performance of this architecture is then analyzed to reveal where performance limitations occur and opportunities for design improvement exist.

2.1 Fundamentals of Thermoelectrics

The fundamentals of thermoelectric transport have been well documented [19, 14, 12, 32, 20]. The explanation here will begin by roughly summarizing the description of [19]. For simplicity, properties are assumed to be temperature independent throughout. Thermoelectric systems operate primarily by leveraging two phenomena: the *Seebeck effect* and the *Peltier effect*. The Seebeck effect describes a relationship between a temperature gradient in a material and an induced electromotive force:

$$S = \frac{E_1 - E_2}{T_1 - T_2} \tag{2.1}$$

The Seebeck coefficient S depends on many material properties and physical conditions, but it is generally possible to find an average, constant value of S for a given application. The Seebeck coefficient can be positive or negative, i.e. the thermal and

electric potential gradients can be in the same or opposing directions. In fact, the Seebeck effect can be controlled through careful design of the material composition and structure. Thermoelectric elements thus can be designed with either positive (*p-type*) or negative (*n-type*) Seebeck coefficients.

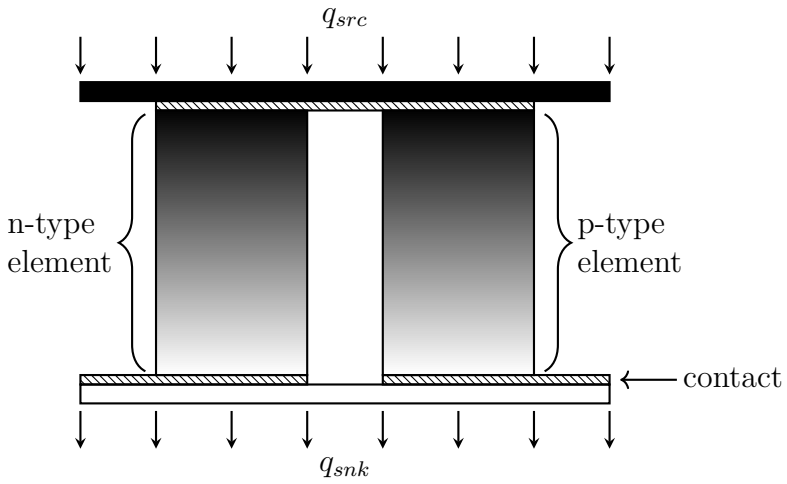

Figure 2-1: Traditional architecture of an n-p pair

The simplest thermoelectric device consists of one p-type and one n-type element (an *n-p pair*). The traditional architecture of an n-p pair is shown in Fig. 2-1. Both elements have the same height and square cross-section. The elements are connected by a thin contact made of a thermally and electrically conductive material, and the remaining space is filled with an insulator (e.g. air). This configuration introduces a second phenomenon related to the Seebeck effect known as the Peltier effect. The Peltier effect states that heat (q_P) is generated or absorbed at the interface of two thermoelectric materials:

$$q_P = I(S_p - S_n)T = IS_{pn}T \tag{2.2}$$

It is worth noting that a third effect, the *Thomson effect*, exists and must be considered if the Seebeck coefficient is not assumed to be temperature independent [20].

These effects are combined with one-dimensional heat transfer theory to form an equivalent thermal circuit for this device (Fig. 2-2). The thermal and electrical resistances of the connectors are assumed to be negligible. The material properties of the

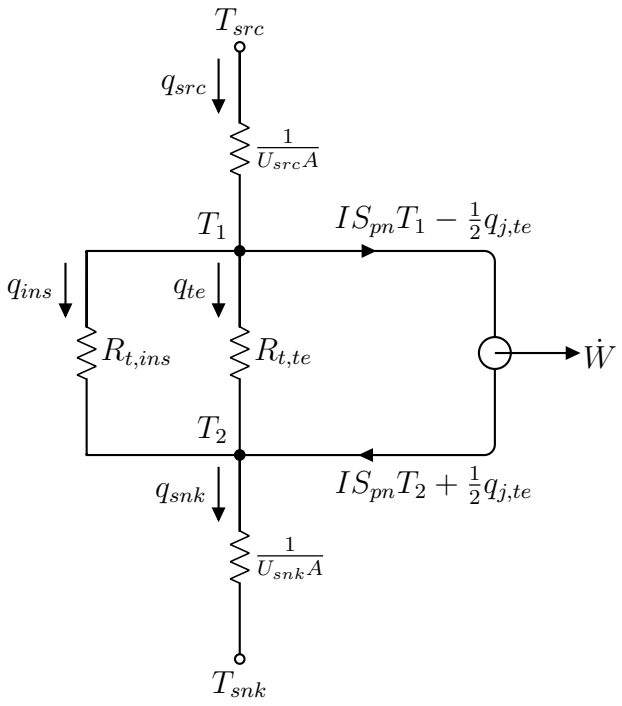

Figure 2-2: Thermal circuit for an n-p pair, traditional architecture

n-type and p-type elements are assumed to be equivalent, save the Seebeck coefficient, which is assumed to be of equivalent magnitude but opposite sign. Convection occurs on both the source and sink sides of the device such that q_{src} and q_{snk} are defined as:

$$q_{src} = U_{src}A(T_{src} - T_1) \qquad q_{snk} = U_{snk}A(T_2 - T_{snk}) \tag{2.3}$$

where U_{src} and U_{snk} are the overall heat transfer coefficients of the convection processes and A_{tot} is the total area of the n-p pair. The thermal resistances (R_t) are recognized to be one-dimensional planar conduction resistances:

$$R_{t,te} = \frac{l_{te}}{k_{te}(2A_{te})} \qquad R_{t,ins} = \frac{l_{te}}{k_{ins}(A - 2A_{te})} \tag{2.4}$$

Joule heating in the elements due to electrical resistance is non-negligible. The electrical resistance (denoted as R_e) and joule heat q_j are described as:

$$R_{e,te} = \frac{l_{te}}{\sigma_{te}(2A_{te})} \qquad q_{j,te} = I^2 R_{e,te} \tag{2.5}$$

where the joule heat q_j is generated uniformly and travels along the vertical axis of the elements only such that the heat is delivered evenly to the end surfaces.

With these definitions, the thermal circuit shown in Fig. 2-2 can be evaluated. In this circuit, T_1, T_2, and I are unknown, so a system of three equations is required to resolve the system. Two equations can be found by balancing the energy flows into and out of the temperature nodes T_1 and T_2:

$$q_{te} + q_{ins} + IS_{pn}T_1 = q_{src} + \frac{1}{2}q_{j,te} \tag{2.6}$$

$$q_{snk} = q_{te} + q_{ins} + IS_{pn}T_2 + \frac{1}{2}q_{j,te} \tag{2.7}$$

The third required equation depends on the configuration of the device as either a generator or refrigerator.

2.1.1 Thermoelectric Generation

In a thermoelectric generator (TEG), an existing temperature gradient is leveraged to generate electric power. Heat flows from the source to the sink in parallel across the elements, and the current induced flows through the elements from the sink-side contact of the n-type element to the sink-side contact of the p-type element. The generated power is transferred to an attached load of known resistance $R_{e,load}$ by connected wire leads:

$$\dot{W} = I^2 R_{e,load} \tag{2.8}$$

Assuming no system losses have been neglected, any power not transferred from the source to the sink as heat must be transferred to the attached load to satisfy conservation principles. Therefore,

$$\begin{aligned}
\dot{W} &= q_{src} - q_{snk} \\
&= q_{te} + q_{ins} + IS_{pn}T_1 - \frac{1}{2}q_{j,te} - q_{te} - q_{ins} - IS_{pn}T_2 - \frac{1}{2}q_{j,te} \\
&= IS_{pn}(T_1 - T_2) - q_{j,te}
\end{aligned}$$

Substituting for $\dot{W}$ and $q_{j,te}$, a relationship for I is obtained:

$$\begin{aligned} I^2 R_{e,load} &= I S_{pn}(T_1 - T_2) - I^2 R_{e,te} \\ \implies 0 &= I^2(R_{e,load} + R_{e,te}) - I S_{pn}(T_1 - T_2) \end{aligned} \tag{2.9}$$

Equations 2.6, 2.7, and 2.9 can be solved simultaneously to resolve the thermal circuit. These equations can easily be applied to a larger module with many thermoelectric couples. Such a system is designed because a singular n-p pair does not usually produce a usable amount of power. The n-p pairs are connected thermally in parallel and electrically in series so the amount of power produced is additive. An example module is illustrated in Fig. 2-3.

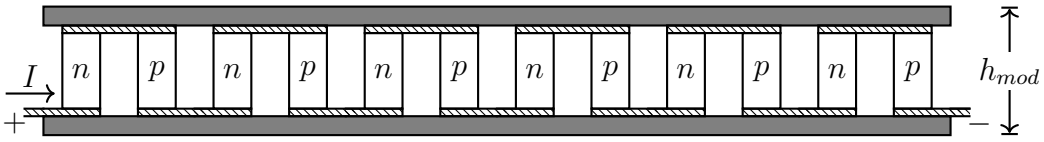

Figure 2-3: Traditional module architecture

The circuit from Fig. 2-2 can adapted for a large module by considering the power output of the module, $\dot{W}_{mod}$. For a module containing N n-p pairs,

$$\begin{aligned} \dot{W}_{mod} &= \sum_{i=1}^{N} \dot{W}_i = N\dot{W} \\ I^2 R_{e,load} &= N\dot{W} \\ \implies \dot{W} &= I^2 \left(\frac{R_{e,load}}{N} \right) \end{aligned} \tag{2.10}$$

Equation 2.10 implies that a large module can be solved on a per-pair basis by dividing the load attached to the module by the total number of n-p pairs. Alternatively, a module can also be solved by re-deriving the relationships previously described for a system of N couples. These methods are mathematically equivalent, but the former will be used henceforth.

2.1.2 Thermoelectric Refrigeration

The thermoelectric effects can also be leveraged in the opposite manner in a thermoelectric cooler (TEC) by driving a current to create a temperature gradient. This theoretically allows for the creation of a refrigerator with no moving parts. The behavior of an n-p pair in a refrigeration system can be modeled by making only a small adaptation to the model of Fig. 2-2. In the generation case, equations 2.6, 2.7, and 2.9 were derived to compute the system's three unknown values, T_1, T_2, and I. Equation 2.9 was derived using an overall power balance and a known $R_{e,load}$.

In a cooling system, however, there is no load resistance attached. Instead, a power supply drives a known current through the system. This current determines how much heat is pumped from the source side, q_{src}. When a known current, I_o, is applied, Equation 2.9 is replaced by Equation 2.11a. Alternatively, one could specify a desired amount of heat to be drawn from the source, then compute the current required to pump this heat. A common application of this method is the case where $q_{src} = 0$ and the cooler must simply pump enough heat to counteract heat leakage into the system. If the source heat flow is specified, then Equation 2.9 is replaced by Equation 2.11b.

$$I = I_o \tag{2.11a}$$

$$q_{src} = q_{src,o} \tag{2.11b}$$

Equations 2.11a or 2.11b, together with Equations 2.6 and 2.7, form a solvable set of equations for a thermoelectric refrigerator. Similar to generation, it is straightforward to adapt the equations to a module made of many n-p pairs.

2.2 Evaluating Performance

Having introduced thermoelectric fundamentals and characterized traditional generators and refrigerators, pertinent performance evaluation metrics can now be considered with proper context.

For generators, a commonly used measure of performance in generation is the efficiency of the device's energy conversion, where the efficiency η of an n-p pair is:

$$\eta = \frac{\dot{W}}{q_{src}} \tag{2.12}$$

For the limiting case where $R_{t,ins} \to \infty$, a maximum efficiency η_{max} can be achieved at a specific load to internal resistance ratio, M [14, 20]:

$$\eta_{max} = \frac{(T_1 - T_2)}{T_1} \cdot \frac{M - 1}{M + {}^{T_2}/_{T_1}} \qquad M = (1 + Z\bar{T})^{1/2} \tag{2.13}$$

where

$$Z = \frac{{S_{pn}}^2}{R_{t,te} R_{e,te}} \qquad M = \frac{R_{e,load}}{R_{e,te}} \tag{2.14}$$

For thermoelectric refrigeration, the coefficient of performance ϕ is of interest and is defined as:

$$\phi = \frac{q_{src}}{\dot{W}} \tag{2.15}$$

Again, for the case where $R_{t,ins} \to \infty$, an analytical maximum ϕ_{max} exists [13]:

$$\phi_{max} = \frac{T_1 \left(\sqrt{1 + Z\bar{T}} - \frac{T_2}{T_1} \right)}{(T_2 - T_1) \left(\sqrt{1 + Z\bar{T}} + 1 \right)} \tag{2.16}$$

For both generation and refrigeration, the performance metrics depend solely on the temperature profile and the dimensionless group $Z\bar{T}$. This revelation has led to significant efforts to improve the Z of thermoelectric materials, which are summarized extensively in [39, 14, 51, 36]. However, η and ϕ are rarely only functions of $Z\bar{T}$, T_1, and T_2 in real-world scenarios. Even in the simple example shown in Fig. 2-2, the thermal properties of $R_{t,ins}$ become relevant when $R_{t,ins} \not\gg R_{t,te}$. $Z\bar{T}$, then, is only part of the larger variable space that affects overall device performance. It determines the upper limit, but the many other relevant parameters determine what performance can be achieved in an actual system. The remainder of the work here

focuses on analyzing and addressing these additional factors. It will show that the traditional thermoelectric module is poorly suited for many physical scenarios and that an alternative system design can greatly improve performance.

2.3 The Importance of Fill Factor

One such relevant parameter is the *fill factor* of the device. Fill factor refers to the geometric ratio of thermoelectric area to the total area of the n-p pair available for conductive heat transfer, A_{te}/A_{tot}. Like the elements themselves, the area available for conductive heat transfer is assumed to have a square cross-sectional area. In a square module of two or more evenly distributed n-p pairs, this is in fact true as repeating heat flux boundaries will occur at regular intervals between the elements. For a module with N n-p pairs, this equates to $N \cdot A_{te}/A_{mod}$ where $A_{mod} = N \cdot A_{tot}$. Fig. 2-4 shows cross sections of a fixed area module with two and eight n-p pairs.

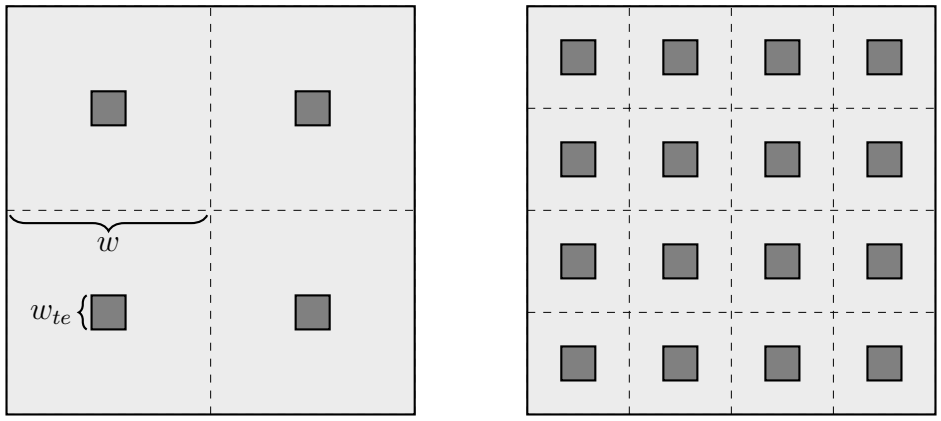

(a) $N = 2$, $\dfrac{A_{te}}{A_{tot}} = \dfrac{1}{36}$ (b) $N = 8$, $\dfrac{A_{te}}{A_{tot}} = \dfrac{1}{9}$

Figure 2-4: Examples of fill factor, cross-sectional view of module

The increase of thermoelectric pairs from two to eight necessarily increases the fill factor of the module. This increase positively affects the performance of each pair as it decreases the available area for flow through the insulator and increases the resistance $R_{t,ins}$. However, higher fill factors also reduce the overall area per couple available for external heat exchange.

Table 2.1: Estimated heat exchanger scenarios

Scenario	U [$\mathrm{W\,m^{-2}\,K^{-1}}$]
Free convection, gas [19]	2–25
Forced convection, gas [19]	25–250
Unducted plate-fin heat exchanger, free convection, gas†	2–350
Unducted plate-fin heat exchanger, forced convection, gas†	25–1500

† Estimates adapted from analysis by Kasey J. Russell, Draper.

It is obvious that heat exchangers with large overall heat exchange coefficients U are desirable. When U is sufficiently large, the area available for heat exchange becomes minimally important, and many couples can be packed tightly to produce maximal power. This fact has led to efforts to understand and achieve favorable heat exchanger performance for thermoelectric modules [50, 7, 11]. Some estimated ranges of U values seen in thermoelectric applications are given in Table 2.1. However, heat exchangers have also been shown to sometimes dramatically increase overall device costs [48] and often require loud, low-reliability components such as pumps and fans.

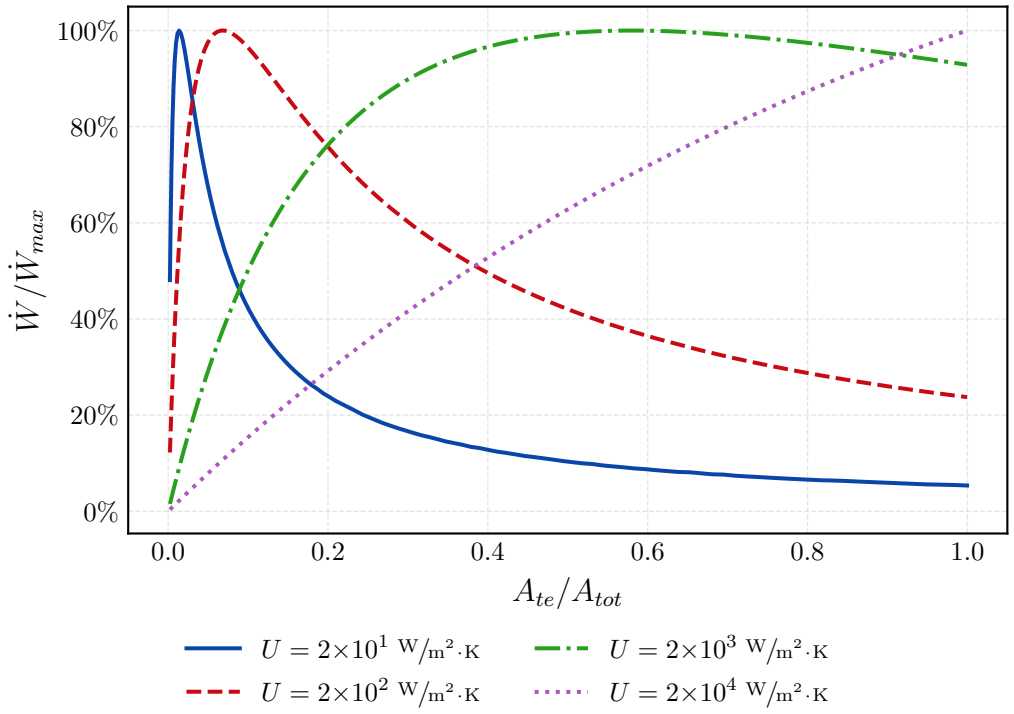

Figure 2-5: Effect of fill factor on power generation, traditional architecture

Due to the shortcomings of heat exchangers, understanding fill factor effects is material to improving system performance – particularly so for low values of U. Fig. 2-5 shows the relative performance of a module modeled by the representation in Fig. 2-2 for various fill factors and overall external heat transfer coefficients ($U = U_{src} = U_{snk}$). It is evident that for low values of U, which are common in waste heat recovery applications, a small fill factor ($< 10\%$) is desirable. A similar conclusion was reached in previous work [47]. The existence of a point of peak power is also evident. When the fill factor is reduced beyond this point, performance decreases because of the relative increase in heat flow through the insulation between elements (illustrated in Fig. 2-6). This thermal short allows heat to bypass the thermoelectric elements, thereby reducing available heat for conversion to electricity. Still, for many applications, the fill factor yielding peak power is lower than the fill factors typically employed in the traditional architecture ($\approx 30\%$)[1]. Optimizing fill factor therefore presents an opportunity to improve performance.

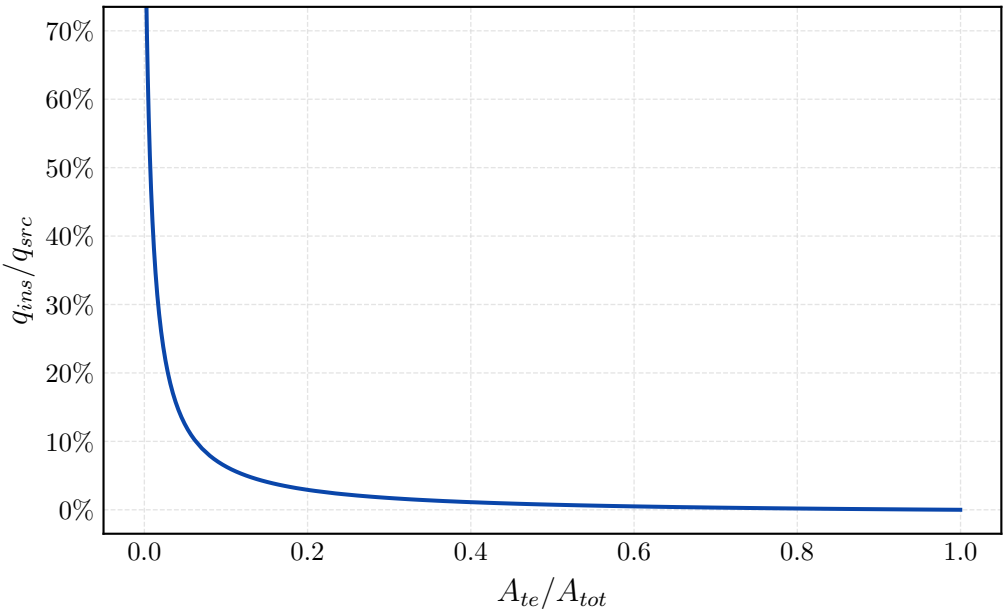

Figure 2-6: Effect of fill factor on heat flow through insulation

[1]Traditional fill factor estimated from datasheet of RC12-2.5 [18].

2.4 Limitations of Low Fill Factor Designs

Two primary issues exist in modules with low fill factors. The first issue is thermal shorting through the insulator, as discussed. The second issue is the thermo-mechanical stresses that are exacerbated in such configurations. All thermoelectric devices are subjected to mechanical stress due to the imposed temperature gradients. Finite-element modeling has been used to simulate these effects, both generally [1, 40] and for real-world applications [6].

For devices subjected to periodic temperature profiles, the cyclic bending due to thermal stresses can also cause fatigue fracturing that degrades performance and causes mechanical failure [3, 16]. Erturun et. al found that configurations with high fill factors and high aspect ratio elements reduce these detrimental stresses [10]. Other work has reached a similar conclusion that the use of long, thin legs would reduce these thermal stresses [38, 52]. However, they also found that the low aspect ratio elements yield greater power output [10], and the previous section here showed that for many values of U low fill factors improve power output. Unfortunately, this implies that device performance and structural integrity are often inversely related.

Interestingly, both of these problems stem from the inherent coupling of thermoelectric element height and total device height. In traditional thermoelectric devices, the structural plates are connected directly to the elements, thereby coupling the device height to the height of the elements. If these heights could be de-coupled, however, both performance and mechanical reliability could conceivably be improved. Elements could be made shorter, wider, and be spaced further apart to improve performance. Then, these elements could be embedded in a much taller structure to mitigate thermo-mechanical stress. Creating, evaluating, and integrating such an architecture into system design is the focus of the remainder of this work.

This page intentionally left blank.

Chapter 3

Distributed Module Architecture

At the end of the previous chapter, lowering the fill factor of a device was shown to improve performance in many conditions. However, issues arise when attempting to reduce the fill factor of a traditionally designed device due to the coupling of the overall device height and the height of the elements. These issues are primarily the thermo-mechanical stresses that fracture the thermoelectric material and the thermal short that occurs through the insulation between elements. In this chapter, a novel distributed architecture is presented to address these issues.

3.1 Single-Element Distributed Architecture

The primary design feature of the distributed architecture is the attachment of wire leads to the thermoelectric elements which enables the distribution of elements flexibly throughout the system (hence the name *distributed*). These wires serve the same purpose as the thin contacts in traditional modules of connecting the elements electrically in series and thermally in parallel. Using wires greatly expands the possible design space by removing geometric and mechanical constraints. Specifically, the height of the device is no longer constrained by the thermoelectric element height because small elements can now be embedded in a larger environment. The wires are also able to bear the mechanical stress associated with the temperature gradients seen in thermoelectric applications.

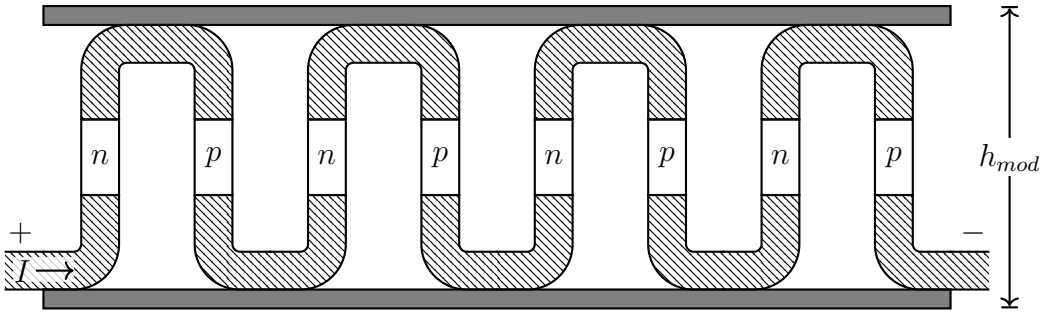

Figure 3-1: Distributed module architecture

Fig. 3-1 depicts an example distributed module and an annotated n-p pair is given in Fig. 3-2 (shaded to illustrate heat transfer). Like the traditional module (Fig. 2-1), top and bottom plates form the structural shell of the device, and insulation fills the remaining space. Instead of connecting the elements to these plates with thin contacts, they are now connected through the attached wires.

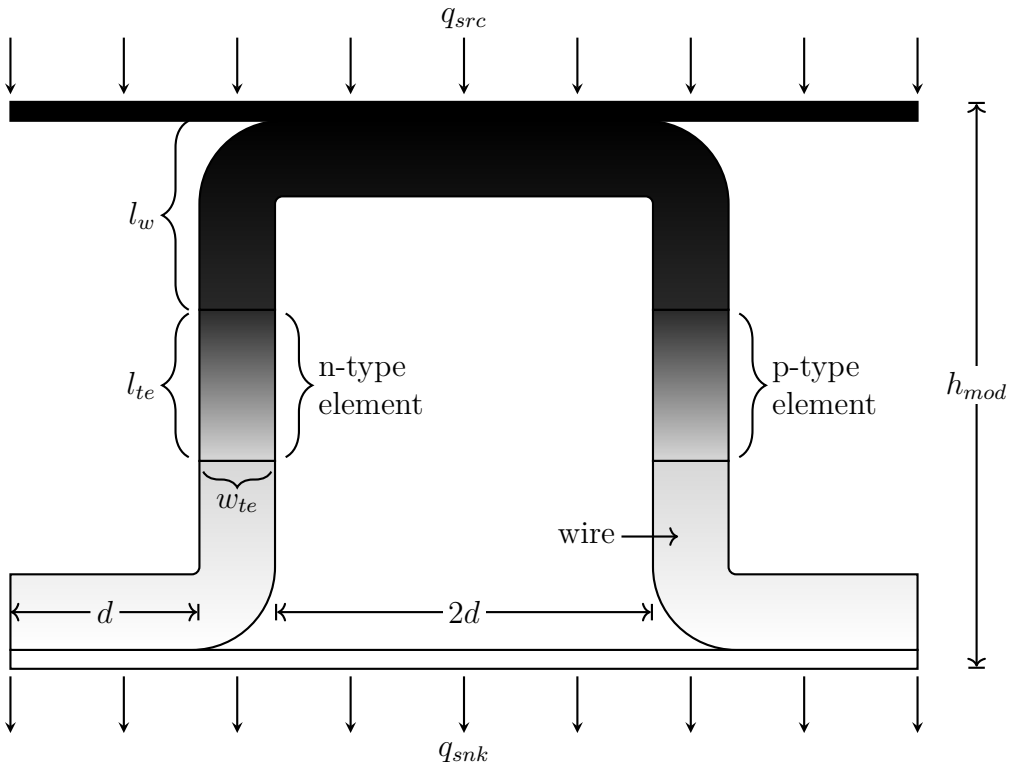

Figure 3-2: Distributed architecture, single n-p pair

A simple thermal circuit that closely represents the distributed module is once again desirable for studying and understanding performance. The use of wires and

the wider distribution of elements in the distributed module requires substantial additions to the thermal circuit. Fig. 3-3 shows the proposed model for the distributed system, which aims to capture as many phenomena as possible while maintaining relative simplicity. Similar to the traditional model, the distributed model simulates a scenario with known external convective cooling conditions. A brief explanation of the additions to the circuit and changes from the traditional circuit model (Fig. 2-2) follows.

The first addition to the model is the inclusion of the thermal resistance of the exterior plates, $R_{t,pl}$. This is often relatively negligible (and therefore ignored in the analysis) but is included here for completeness. The plate resistance is defined as

$$R_{t,pl} = \frac{l_{pl}}{k_{pl} A_{tot}}. \tag{3.1}$$

The thermal effects of the wires are also added. For simplicity, the wires are assumed to have a square cross-section. The wire resistances are defined as:

$$R_{t,w} = \frac{l_w}{k_w 2A_w} \qquad R_{e,w} = \frac{l_w}{\sigma_w 2A_w} \qquad q_{j,w} = I^2 R_{e,w} \tag{3.2}$$

The insulation resistance, $R_{t,ins}$, has simply been generalized from the traditional model where it was specified to be air in $R_{t,air}$. Note that the insulation path does not include the negligible conductive resistances of the horizontal wire sections attached directly to the plates. However, there is a spreading resistance for heat flowing between the plates and contacting wires. This is modeled as an equivalent resistance $R_{t,s}$ (see Section 3.3). Thermal contact resistances have been introduced and are denoted by $R_{t,c}$ and subscripts which identify the two interfacing components. Finally, a three-dimensional effect known as *thermal fringing* carries heat directly between the wires and around the element itself. This phenomenon is modeled as an effective resistance $R_{t,fr}$ that is derived in detail in Section 3.2.

The same method used to resolve the traditional model can be applied here to the distributed model. In this model, there are nine unknowns: eight temperature nodes and the current. A system of nine independent equations is therefore required. Eight

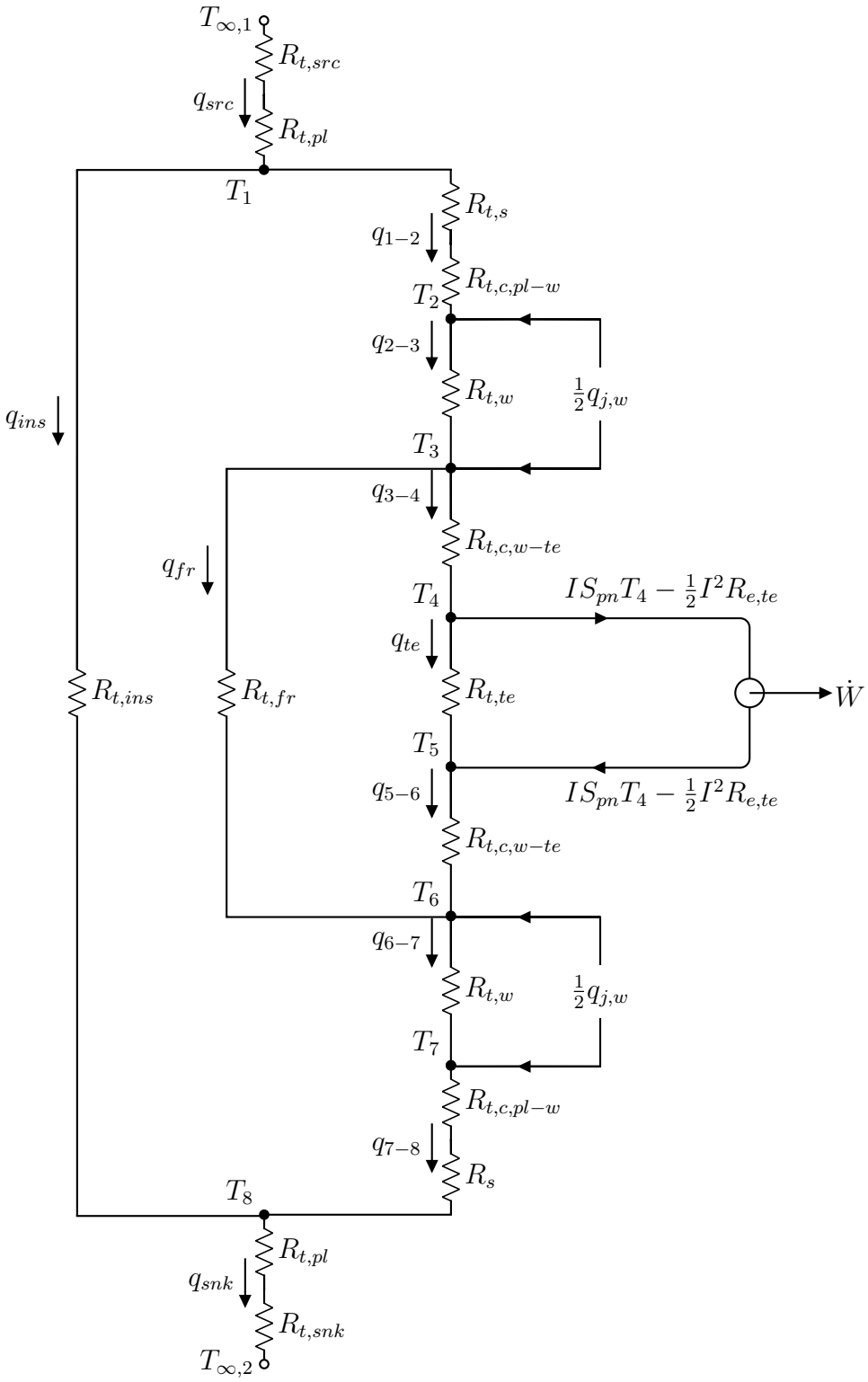

Figure 3-3: Thermal circuit for an n-p pair, distributed architecture

equations can be found by balancing the heat flows at the temperature nodes:

$$q_{12} + q_{ins} = q_{src} \tag{3.3}$$

$$q_{23} = q_{12} + \frac{1}{2}q_{j,w} \tag{3.4}$$

$$q_{34} + q_{fr} = q_{23} + \frac{1}{2}q_{j,w} \tag{3.5}$$

$$q_{te} + IS_{pn}T_4 = q_{34} + \frac{1}{2}q_{j,te} \tag{3.6}$$

$$q_{56} = q_{te} + IS_{pn}T_5 + \frac{1}{2}q_{j,te} \tag{3.7}$$

$$q_{67} = q_{56} + q_{fr} + \frac{1}{2}q_{j,w} \tag{3.8}$$

$$q_{78} = q_{67} + \frac{1}{2}q_{j,w} \tag{3.9}$$

$$q_{snk} = q_{78} + q_{ins} \tag{3.10}$$

As discussed in Chapter 2, the final equation differs for generators and refrigerators. For a generator, the power produced depends on the overall heat exchange and the attached load resistance, which reduces to the simple relationship

$$\begin{aligned} \dot{W} = q_{src} - q_{snk} &= IS_{pn}(T_4 - T_5) - q_{j,te} \\ I^2R_{e,load} &= IS_{pn}(T_4 - T_5) - I^2R_{e,te} \\ \implies 0 &= I^2(R_{e,load} + R_{e,te}) - IS_{pn}(T_4 - T_5) \end{aligned} \tag{3.11}$$

For a refrigerator, a known current I_o or a desired source heat flow q_{src} are specified as in Equations 2.11a and 2.11b. Equations 3.3–3.10, together with the appropriate power relationship (Equation 3.11, 2.11a, or 2.11b) form a complete set of equations.

However, the distributed architecture has introduced additional modes of parasitic heat transfer - thermal fringing ($R_{t,f}$) and thermal spreading ($R_{t,s}$) - that are at present undefined. The relative magnitude of these new parasitic loads and the benefits gained from the distributed architecture will determine whether the architecture improves overall performance. The next two sections are dedicated to understanding these phenomena and resolving $R_{t,s}$ and $R_{t,fr}$ so that the system can be evaluated.

3.2 Thermal Fringing

Thermal fringing occurs when gap of relatively low thermal conductivity is present in a long, thin solid of relatively high thermal conductivity (e.g. the wiring in the distributed module). The gap impedes the flow of heat through the solid and consequently some of the heat is redirected around the solid. In the distributed thermoelectric module, this is detrimental to performance as it effectively increases the thermal conductance of the element and reduces the temperature difference across the element. Thus, quantifying and understanding the behavior of this phenomenon is essential to improve module performance.

A simple way to visualize this phenomenon is to consider the magnetic flux lines in a C-shaped magnet. The air gap present in the magnet has low permeance relative to the rest of the magnet, and thus some of the magnetic field will travel in a path around the gap. This comparison is not only useful for intuition and visualization. Mathematically, the concepts of magnetic permeance and thermal conductance are analogous and therefore a method useful for resolving magnetic permeance can applied to thermal transport. In fact, minimal research on thermal fringing itself exists; one of the prevailing methods for modeling thermal fringing is simply an adaptation of a method developed by H.C. Roters in 1970 to model magnetic permeance around an air gap [31]. Analysis and validation of Roters' method and its application to thermal fringing is therefore a logical and useful starting place for understanding thermal fringing in the distributed module.

3.2.1 Roters' Method for Calculation of Permeance

H. C. Roters presents a method for calculating the magnetic permeance of an air gap in his book, Electromagnetic Devices [31]. Roters seeks to calculate the magnetic permeance of air gaps between two highly permeable surfaces. Magnetic permeance, defined in Eqn. 3.12, is a function of the permeability constant μ and geometry. To resolve the permeance of a gap with a finite cross-sectional area, Roters employs what he calls the *Method of "Estimating the Permeances of Probable Flux Paths."*

The method first defines a probable area through which magnetic flux lines flow. Then, the mean length flux line is calculated and applied as the characteristic length in the permeance relationship. This method, Roters argues, is fairly accurate because the net error associated with using the mean length flux line has expectation zero.

$$P = \mu \frac{A}{g} \tag{3.12}$$

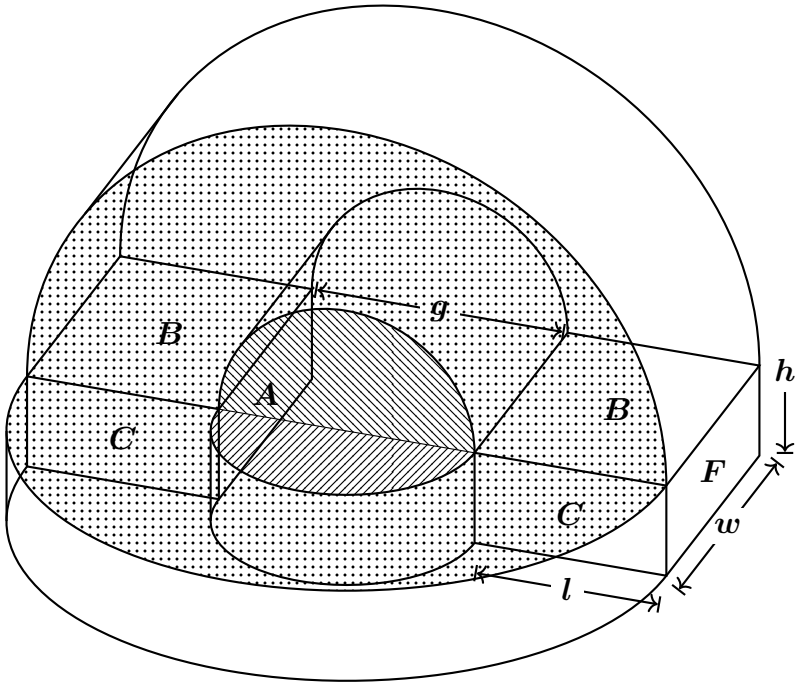

Figure 3-4: Roters' geometry for calculation of permeance

Figure 3-4 shows the specific geometry in question. Two rectangular prisms exist in an infinite space with a defined gap between them. Faces D and E (hidden) are opposite faces B and C, respectively. Using the method of estimating probable flux paths, Roters resolves the half cylinders, annuli, and spherical shells surrounding the gap to estimate a net geometry of permeance. The permeance relationship for the semicircular cylinders about the edges AB, AC, AD, and AE is:

$$P_{1,top} = 0.264\mu w \qquad\qquad P_{1,side} = 0.264\mu h \tag{3.13}$$

For the half annuli about faces B, C, D, and E, the permeance is:

$$P_{2,top} = \begin{cases} \dfrac{\mu w}{\pi} \ln\left(1 + \dfrac{2l}{g}\right) & g \leq 3l \\ \dfrac{2\mu w}{\pi\left(\dfrac{g}{l} + 1\right)} & g > 3l \end{cases} \qquad P_{2,side} = \begin{cases} \dfrac{\mu h}{\pi} \ln\left(1 + \dfrac{2l}{g}\right) & g \leq 3l \\ \dfrac{2\mu h}{\pi\left(\dfrac{g}{l} + 1\right)} & g > 3l \end{cases} \tag{3.14}$$

For the spherical quadrants about corners ABC, ACD, ADE, and AEB:

$$P_3 = 0.077\mu g \tag{3.15}$$

And, for the shells about edges BC, CD, DE, and EB:

$$P_4 = 0.25\mu l \tag{3.16}$$

The permeances are summed for all four sides, yielding the total permeance:

$$P_{tot} = 4\left(P_1 + P_2 + P_3 + P_4\right) \tag{3.17}$$

As previously mentioned, thermal conductance is analogous to magnetic permeance. By substituting thermal conductivity, k, for magnetic permeability, μ, Roters' method can be adapted to thermal conductance. The analogous relationships are given in Equation 3.18. To simplify this and further calculations, the prisms and gap are henceforth assumed to be square, i.e. $l = h$.

$$K_1 = 0.264kw \qquad K_2 = \begin{cases} \dfrac{kw}{\pi} \ln\left(1 + \dfrac{2l}{g}\right) & g \leq 3l \\ \dfrac{2kw}{\pi\left(\dfrac{g}{l} + 1\right)} & g > 3l \end{cases}$$

$$K_3 = 0.077kg \qquad K_4 = 0.25kl$$

$$K_{fr} = 4\left(K_1 + K_2 + K_3 + K_4\right) \tag{3.18}$$

It is therefore apparent that $K_{fr} = f(k, w, g, l)$.

Conductance has the dimensions of power per temperature. Given the relationships above, it is easy to non-dimensionalize the fringing conductance by dividing K_{fr} by a length scale, w, and the thermal conductivity, k. Eqn. 3.19 shows the non-dimensional conductance components.

$$\frac{K_1}{kw} = 0.264 \qquad \frac{K_2}{kw} = \begin{cases} \frac{1}{\pi}\ln\left(1+\frac{2l}{g}\right) & g \le 3l \\ \frac{2}{\pi\left(\frac{g}{l}+1\right)} & g > 3l \end{cases}$$

$$\frac{K_3}{kw} = 0.077\left(\frac{g}{w}\right) \qquad \frac{K_4}{kw} = 0.25\left(\frac{l}{w}\right) = 0.25\left(\frac{l}{g}\right)\left(\frac{g}{w}\right)$$

$$\Phi = \frac{K_{fr}}{kw} = 4\left(\frac{K_1}{kw} + \frac{K_2}{kw} + \frac{K_3}{kw} + \frac{K_4}{kw}\right) \tag{3.19}$$

It is evident that $\Phi = f\left(g/w, l/g\right)$. The parameter g/w is the aspect ratio of the gap and the parameter l/g is the ratio of the prism length to the gap length. The non-dimensional fringing conductance Φ can be related to these ratios. Figure 3-5 maps the fringing conductance over a wide range. Φ appears to grow rapidly as g/w and l/g both increase above ≈10.

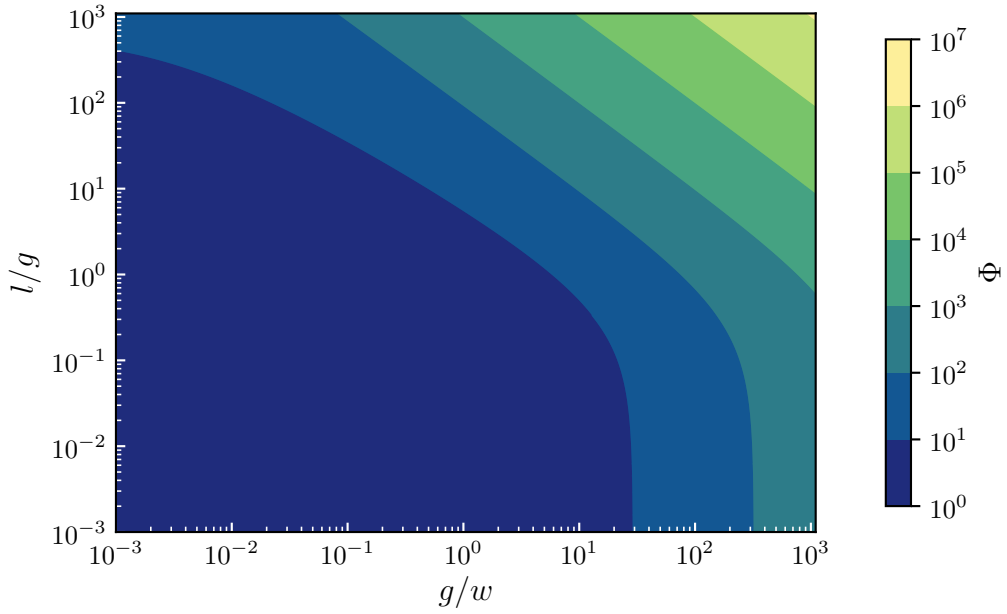

Figure 3-5: Relationship of Φ to geometric ratios

The importance of the fringing is not immediately apparent just from observing Φ. It is more insightful to consider the relative significance of fringing conductance to the conductance through the gap. The non-dimensional gap conductance Λ can be defined in the same manner as the fringing conductance (Equation 3.20). Note that the conductivity of the gap and surrounding area are equivalent in Roters' method – this idea will be reconsidered later as it is often not the case in the distributed system.

$$K_{gap} = \frac{kA}{g} = \frac{kw^2}{g}$$
$$\implies \Lambda = \frac{K_{gap}}{kw} = \frac{w}{g} = \left(\frac{g}{w}\right)^{-1} \tag{3.20}$$

Figure 3-6 shows the ratio of the two non-dimensional quantities, which appears to be strongly dependent on aspect ratio. This accords with intuition and Roters' assertion: as $g/w \to 0$, gap conductance increases so that all the heat is transported through the gap and $\Phi/\Lambda \to 0$. Conversely, as $g/w \to \infty$, gap conductance becomes negligible relative to the fringing conductance and $\Phi/\Lambda \to \infty$.

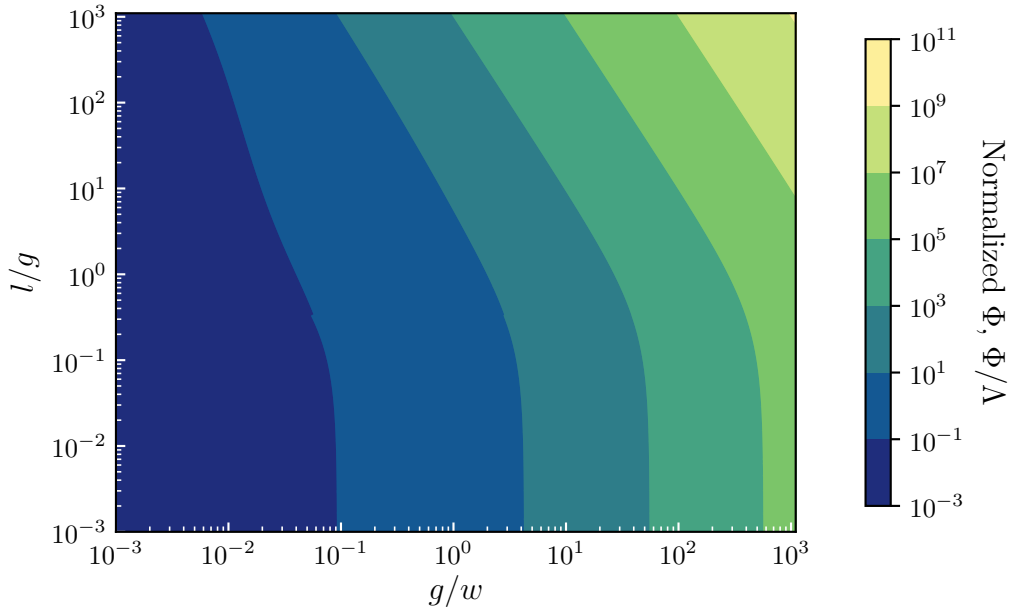

Figure 3-6: Relative magnitude of Φ

The aspect ratio range presented in Fig. 3-6 is rather large for most real-world applications. To gain a better sense for more realistic scenarios, the aspect ratio range

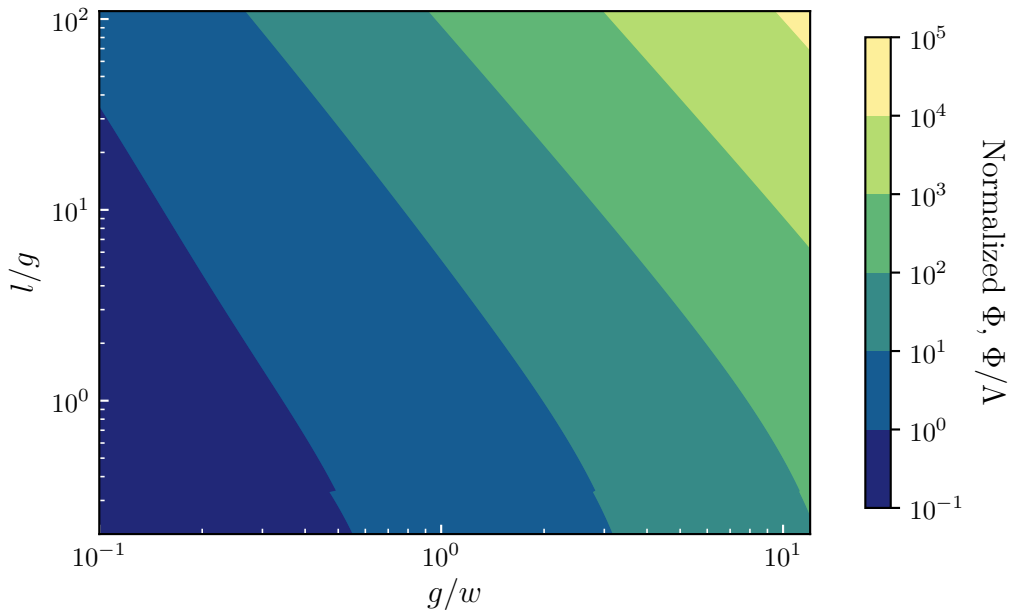

Figure 3-7: Relative magnitude of Φ, limited geometric range

is restricted to two orders of magnitude and the length ratio range to three orders of magnitude. From Figure 3-7, it is evident that a large design space exists where fringing is either negligible or on the order of the gap conductance.

3.2.2 Comparison of Roters' and Numerical Methods

It is valuable to compare Roters' technique with a finite-element model (FEM). Finding a similar relationship would both validate the numerical technique and reveal any systematic error in the Roters' calculation. Roters' condition was simulated with COMSOL Multiphysics® by fixing two wires at different temperatures with a gap of much lower thermal conductivity between them. A wide domain of 5x the total height with the same thermal conductivity as the gap was constructed around the wires and gap. A steady state numerical solution was found and a cut plane was integrated across to find the total heat flow. The heat flow through the gap was also calculated through numerical integration and compared to the theoretical gap heat flow. The numerical heat flow was within 0.2% of the theoretical heat flow for all simulated geometries. Given that the wires maintain a constant temperature, the

difference between the total heat flow and gap heat flow yields the fringing heat flow. The simulated fringing heat flow is then made non-dimensional, Φ_{sim}:

$$\Phi_{sim} = \frac{q_{fr,sim}}{\Delta T \cdot kw} \tag{3.21}$$

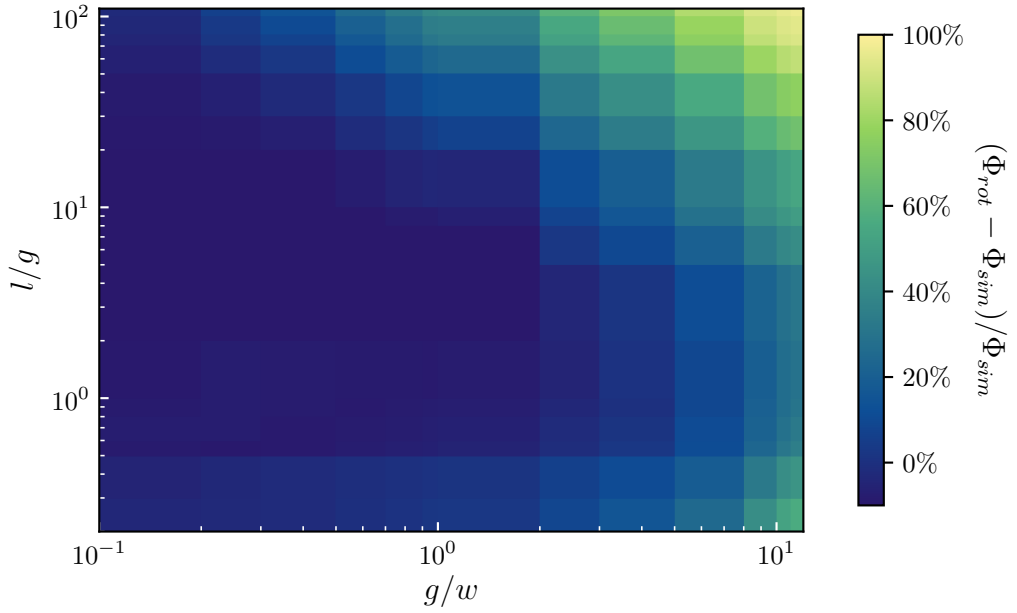

Figure 3-8: Relative difference of Roters' method and numerical simulations

Figure 3-8 shows relative difference between the numerical simulation and Roters' method. The variable space simulated and compared here is more constrained than the space shown in Figure 3-7 because COMSOL Multiphysics® struggles to mesh and calculate the more extreme geometries. Roters' method calculates fringing fairly accurately ($\approx \pm 10\%$) when w, g, and l are all of a similar magnitude and wherever $g/w < 1$. Roters had developed his approximation to model magnetic permeance around air gaps - a scenario where these conditions are met. Outside of this space, however, Roters' approximation overestimates fringing conductance. These more extreme dimensions are part of the distributed architecture's anticipated design space, so another method must be developed to characterize fringing.

3.2.3 Numerical Method for Parameterizing Fringing

The analysis of the previous section suggests that Roters' approximation method will be inaccurate over much of the wide range of possible dimensions in the distributed module. Additionally, other differences between the distributed module and Roters' geometry may impact the fringing conductance. They are summarized as follows:

1. The geometric space for the distributed module may extend into ranges where Roters' approximation is inaccurate (discussed in previous section).

2. In the distributed module, the exterior plates to which the wires are attached also transfer heat. These are not accounted for in Roters' calculations.

3. The wire temperatures are not fixed and are not constant in the distributed module as they are assumed to be in Roters' scenario.

4. With Roters' method, the conductivity of the gap and the surrounding area are the same. In the distributed module, the conductivity of the gap is likely to be greater than the surrounding area by one or two orders of magnitude.

5. The elements in the distributed module may be positioned in close proximity, which will introduce heat flux boundaries that may reduce fringing. Roters' method does not account for a defined boundary around the geometry.

Given the apparent inaccuracies of Roters' method and these additional complexities, it would be difficult to construct an accurate analytical model of fringing for the distributed system geometry. Instead, finite element models of the system are again employed to generate a parameterization. A simplified version of a unit of the distributed module is simulated in a large domain with a width that scales at a constant five times the height, similar to the numerical study conducted for the Roters' method comparison. The top and bottom surfaces of the domain are fixed at constant temperatures to simulate steady-state conditions. The heat flow through a centered cut plane is calculated from the simulation and divided by the specified temperature gradient to yield the overall conductance $K_{t,net}$. A simplified distributed

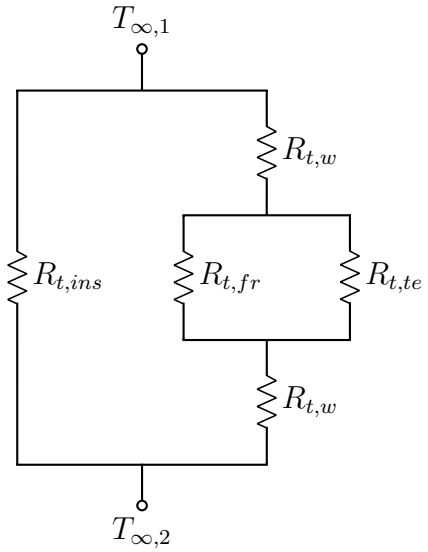

Figure 3-9: Equivalent thermal circuit for numerical simulation case

thermal circuit representing the simulation case (Fig. 3-9) can then be resolved to find the fringing conductance $K_{t,fr}$:

$$K_{t,net} = K_{t,ins} + \frac{1}{2/K_{t,w} + 1/(K_{t,te} + K_{t,fr})}$$

which can be rearranged to yield the fringing conductance:

$$\frac{1}{R_{t,fr}} = K_{t,fr} = \frac{1}{1/(K_{t,net} - K_{t,ins}) - 2/K_{t,w}} - K_{t,te} \tag{3.22}$$

and can again be non-dimensionalized via thermal conductivity and element width:

$$\Phi = \frac{K_{fr}}{kw} = \frac{K_{t,fr}}{k_{ins} w_{te}} \tag{3.23}$$

The value of Φ is now known for all simulated combinations of l_{te}/w_{te} (analogous to g/w) and l_w/l_{te} (analogous to l/g). However, a continuous function within the parameter space is desired so that the relationship can be included in the optimization software. A basis spline can be used to create such a function from the simulation's data points. A small correction was applied to the spline fit for very small values of g/w and l/g, where the fit was overestimating. Figure 3-10 shows a well-conditioned

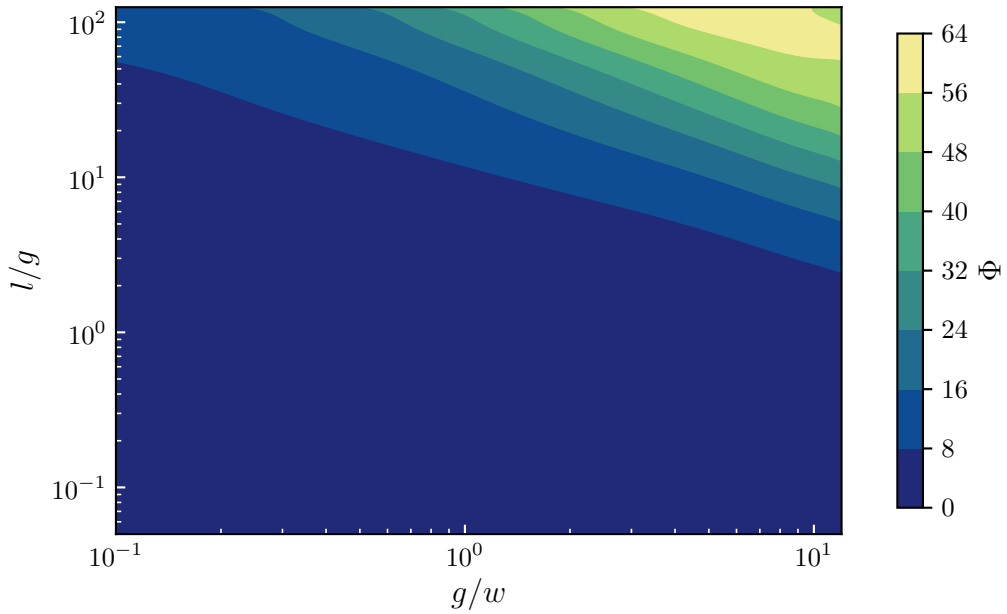

Figure 3-10: Basis spline fit for fringing created from numerical simulations

basis spline fit to the data. Figure 3-11 shows the relative error between the spline fit and the calculated points. For the majority of the design space presented, the error in the fit is within $\approx \pm 20\%$. Error reaches nearly 50% for small values of l/g, but the value of Φ is nearly negligible in this range regardless.

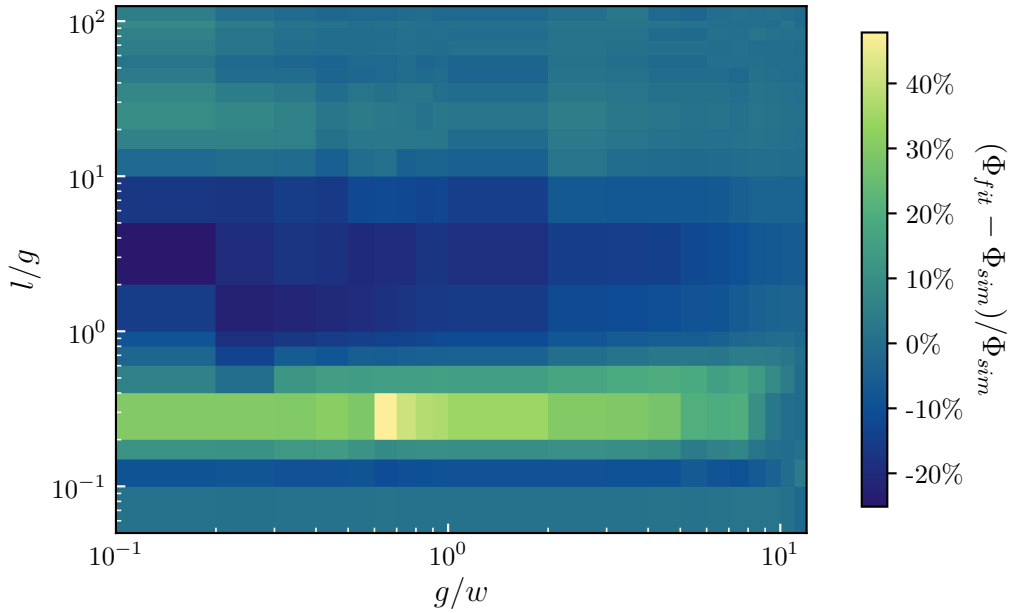

Figure 3-11: Relative error of basis spline fit

3.2.4 Effects of Domain Width

The proximity of an element to its neighbors must also be considered when modeling fringing. Consider the illustration of Fig. 3-12. The dotted line represents the expected outward area (defined by the radius r) where fringing occurs around the wire. The dashed line to the right represents the thermal boundary that occurs halfway between repeated elements at a distance d from the edge of the element (see also Fig. 3-2). When elements are spaced far apart relative to the total height, fringing flow can access the entire area and is maximized. As the space between elements is decreased, the repeating boundary begins to impede the area available for fringing. As $d/r \to 0$, it is expected that $R_{t,fr} \to 0$.

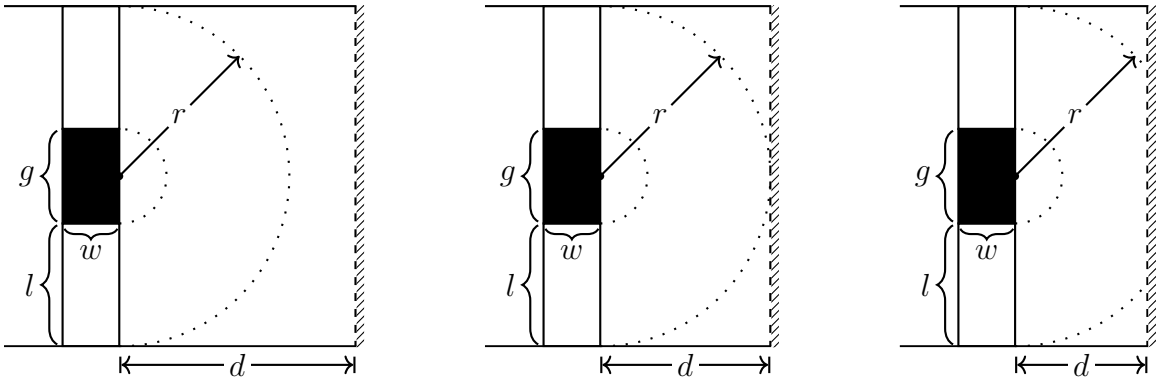

(a) $d/r > 1$ (b) $d/r = 1$ (c) $d/r < 1$

Figure 3-12: Effect of boundary wall distance on available fringing area

Numerical simulations were again employed to model the effects of the boundary wall. A simulation was run for many configurations of g/w and l/g, sweeping over a range of d for each configuration by enforcing vertical repeating heat flux boundaries around the element. The data points on Fig. 3-13 show simulation results for a sample of configurations and the effect of altering the boundary wall location on the fringing conductance. The y-axis shows the fringing conductance relative to the fringing conductance where $d/r = 2$ as it is assumed that fringing is unaffected by the boundary when the boundary is double the radius of expected fringing area.

To model the effects of domain width in the optimization software, a continuous function is required. The data points suggest that conductance and the boundary

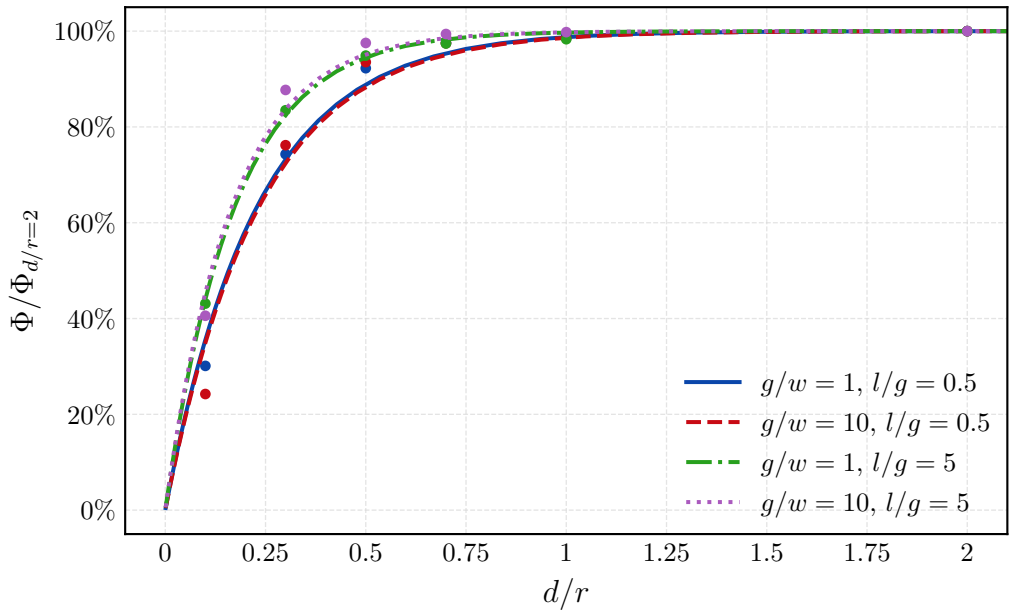

Figure 3-13: Effect of flux boundary on fringing with exponential fits

wall distance may be related exponentially. This apparent exponential relationship can be leveraged as a starting point for finding a function relationship. The function given in Equation 3.24 was used to fit the data, where the rate parameter b was determined for each simulated configuration of g/w and l/g.

$$\frac{\Phi}{\Phi_{max}}\left(\frac{g}{w}, \frac{l}{g}\right) = 1 - \exp\left(-b \cdot \frac{d}{r}\right) \tag{3.24}$$

The fitted curves for the same sample are also shown in Fig. 3-13. While the fits could be improved by adding more parameters, a fit with minimal parameters is desirable because all parameters must subsequently be fit with a basis spline to g/w and l/g. Fitting multiple parameters compounds the error and may actually result in worse accuracy overall. A basis spline was fit to the parameter b with a relative error of $\approx \pm 20\%$, which resulted in an overall relative error of $\approx \pm 10\%$ for a majority of the parameter space (error does approach $\approx \pm 50\%$ where $l/g < 1$, but fringing is small for such dimensions).

3.3 Spreading Resistance

When two objects of similar cross-sectional area are in contact, heat flows in simple one-dimensional conduction. However, if the cross-sections differ, the heat cannot immediately access all the larger cross section's area but instead must *spread* throughout the larger object (illustrated in Fig. 3-14). Such a situation occurs in the distributed architecture where the wires contact the exterior plates. This spreading effectively increases the overall thermal resistance. *Spreading Resistance* captures this resistance in a single value, $R_{t,s}$, that can then simply be added in series to the one-dimensional resistance.

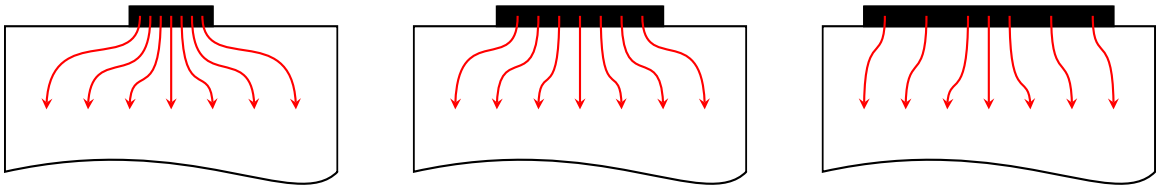

(a) Small source (b) Moderate source (c) Large source

Figure 3-14: Illustrations of spreading for various heat source geometries

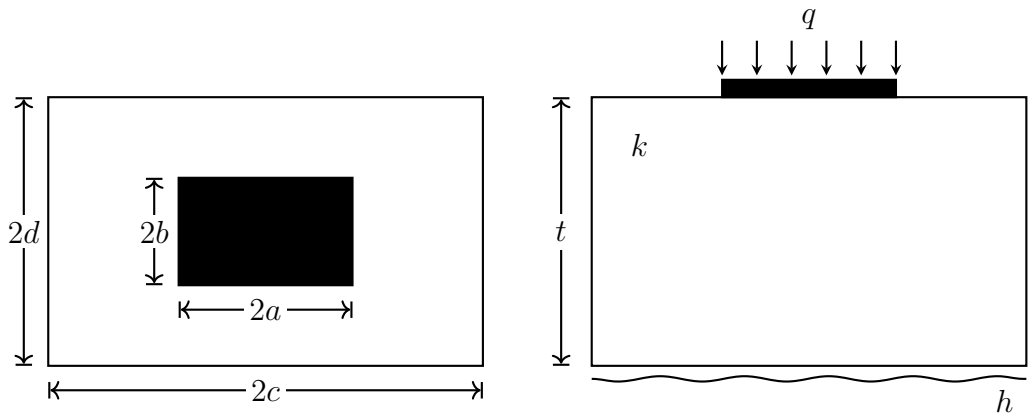

(a) View of Cross-Section (b) Perpendicular View

Figure 3-15: Finite isotropic channel with rectangular heat source (see [49])

Analytical spreading resistance solutions for many geometric configurations are both derived and compiled in [49]. One of the geometries considered, a finite isotropic channel with a rectangular heat source, replicates the scenario of the thermoelectric

distributed module. Fig. 3-15 shows the geometry as defined in [49]. For this geometry, R_s was found to be:

$$R_s = \frac{1}{2a^2cdk}\sum_{m=1}^{\infty}\frac{\sin^2(a\delta_m)}{{\delta_m}^3}\cdot\psi(\delta_m) + \frac{1}{2b^2cdk}\sum_{n=1}^{\infty}\frac{\sin^2(b\lambda_n)}{{\lambda_n}^3}\cdot\psi(\lambda_n) + \frac{1}{a^2b^2cdk}\sum_{m=1}^{\infty}\sum_{n=1}^{\infty}\frac{\sin^2(a\delta_m)\sin^2(b\lambda_n)}{{\delta_m}^2{\lambda_n}^2\beta_{m,n}}\cdot\psi(\beta_{m,n}) \tag{3.25}$$

where the eigenvalues δ_m, λ_n, and $\beta_{m,n}$ are defined as:

$$\delta_m = \frac{m\pi}{c} \qquad \lambda_n = \frac{n\pi}{d} \qquad \beta_{m,n} = \sqrt{{\delta_m}^2 + {\lambda_n}^2} \tag{3.26}$$

and the function $\psi(\zeta)$ is:

$$\psi(\zeta) = \frac{\zeta(e^{2\zeta t}+1) - (1-e^{2\zeta t})h/k}{\zeta(e^{2\zeta t}-1) + (1+e^{2\zeta t})h/k} \tag{3.27}$$

These equations can be applied to the distributed model (Fig. 3-3) where the equivalent variables are substituted as described in Table 3.1.

Table 3.1: Equivalent spreading geometry variables

Fig. 3-15	$2a$	$2b$	$2c$	$2d$	t	q	k	h
Model	$2d$	w_w	w_{pl}	w_{pl}	l_{pl}	q	k_{pl}	U

3.4 Split-Element Distributed Architecture

The distributed architecture could enable the placement of multiple elements in series on a single wire, should the use of multiple elements prove to be advantageous. Here, only the placement of two elements on a wire is considered, though placement of three or more elements on a wire is also an option. Fig. 3-17 illustrates a few two-element configurations. The two-element configurations are considered as the *splitting* of a single element into two halves. The halves are joined by a third piece of wire to transmit heat between the elements. The elements are spaced symmetrically along

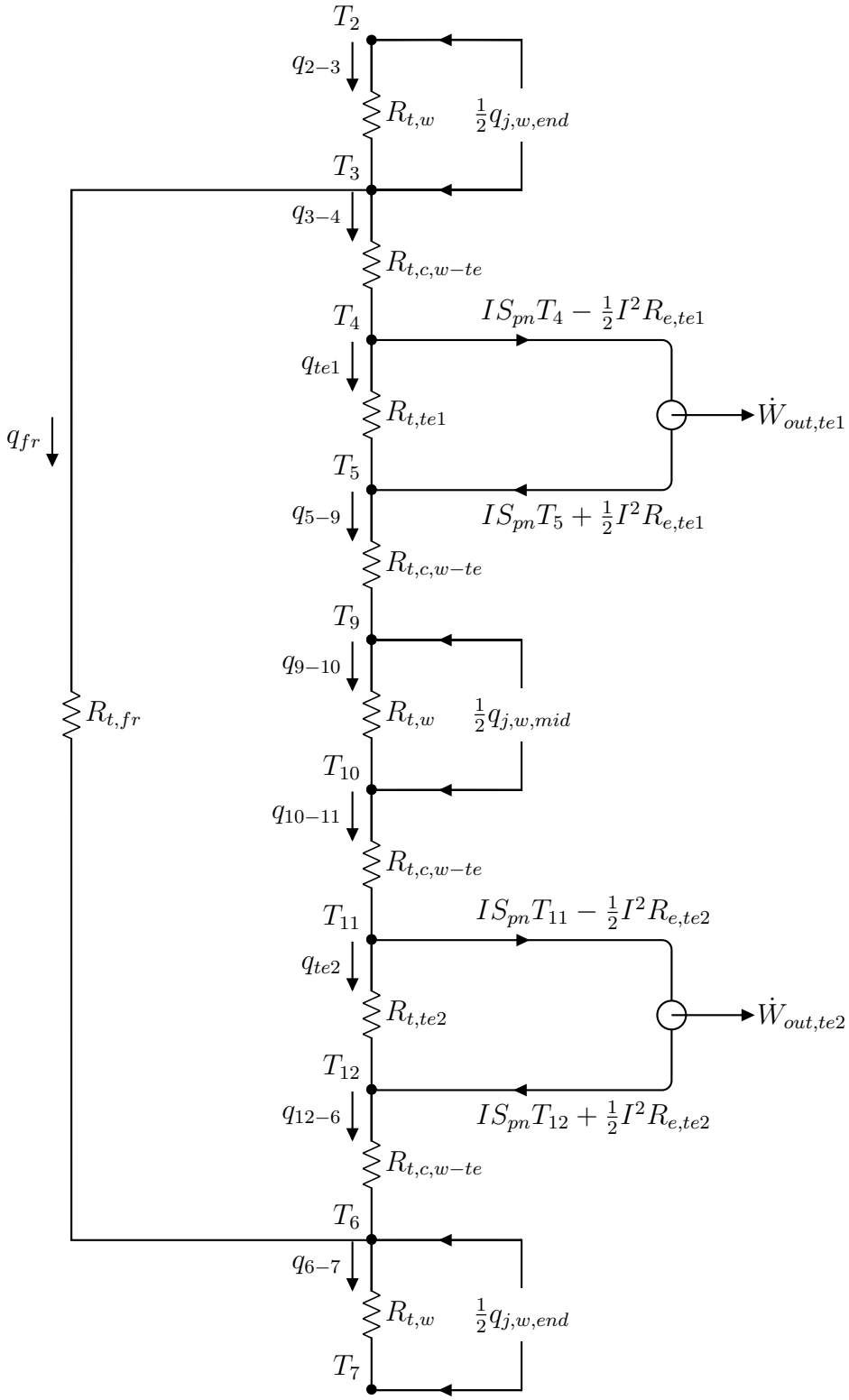

Figure 3-16: Model modification for split-element distributed architecture

the wire, and the spacing between the elements can be varied by adjusting the length of the middle section of wire, $l_{w,mid}$.

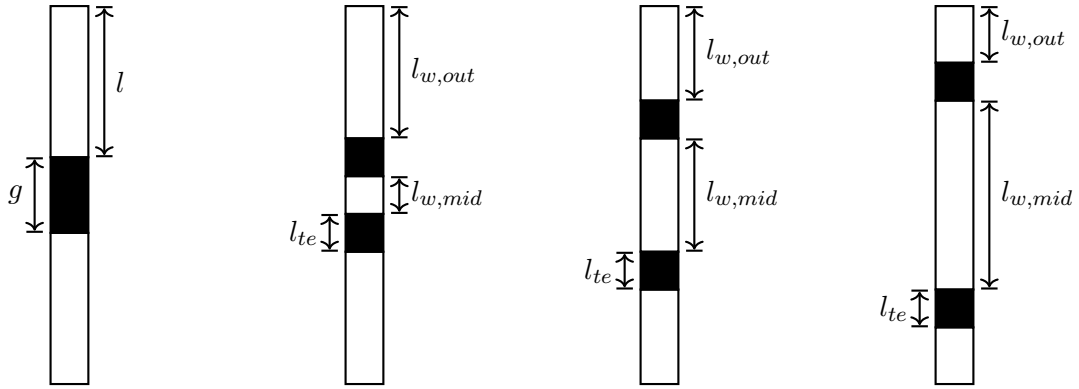

(a) Single-element (b) Split-element

Figure 3-17: Illustrations of split-element geometries

To determine whether the split-element configuration is indeed advantageous to performance, a thermal circuit can again be used to evaluate performance. Initially, it is assumed that the elements are of the same material (with the same temperature independent properties) and that the materials are *fully compatible* (addressed later in the chapter). The distributed model given for a single element in Fig. 3-3 can be modified for the split-element design. The modification is shown in Fig. 3-16. The exterior behavior of the system remains similar to the single-element design, as none of the external conditions or insulating parameters have been altered. The changes to the circuit all occur between the T_3 and T_6 nodes, where a wire and contact resistances have been added.

From a high-level examination of the circuit, only new parasitic heat loads that will hinder performance have been introduced. However, splitting the elements will affect the fringing flow pattern around the elements. If fringing is reduced, $R_{t,fr}$ increases and more heat is directed through the elements. If the benefit from such decreased fringing outweighs the new parasitic losses, performance will improve overall. Thus, it is again pertinent to understand fringing heat flow across the parameter space.

3.4.1 Fringing in the Split-Element Architecture

Like the single-element architecture, a numerical method is used to characterize fringing. To make comparison straightforward, the fringing geometry parameters are defined to be equivalent to the single-element case and are given in Table 3.2.

Table 3.2: Equivalence of variables in discussed fringing configurations

Configuration	Figure Variable				
	g	l	w	d	r
Single-Element	l_{te}	$l_{w,out}$	w_{te}	$w_{mod} - \frac{w_{te}}{2}$	$l_{w,out} + \frac{l_{te}}{2}$
Split-Element	$2l_{te}$	$\frac{2l_{w,out} + l_{w,mid}}{2}$	w_{te}	$w_{mod} - \frac{w_{te}}{2}$	$l_{w,out} + l_{te} + \frac{l_{w,mid}}{2}$
Roters' Method	g	l	w		

It is assumed that the fringing heat is lost to both of the elements, so the fringing flow path is drawn around the outside of the elements. This enables easier analysis and also encompasses the worst-case fringing scenario. Parameterizing fringing for the two element case is significantly more challenging than the single-element case because a new free dimension, $l_{w,mid}$ has been added. This length can also be considered non-dimensionally as a fraction of the total wire length according to the relationship:

$$c = \frac{l_{w,mid}}{l_{w,tot}} = \frac{l_{w,mid}}{l_{w,mid} + 2l_{w,out}} \tag{3.28}$$

The additional dimension c makes numerical simulation more lengthy and time consuming but not impossible. For every configuration in the defined space of g/w and l/g, the range of c must now be considered. While this three-dimensional space is possible in simulation, it cannot be easily fit to a continuous function with a basis spline. Because the continuous function is required to use the model with optimization software (and desired), this issue must be addressed. Ideally, an analytical relationship between the parameter c and fringing behavior independent of g/w and l/g could be deduced, but even cursory analysis of simulation results indicated that such a relationship was likely nonexistent.

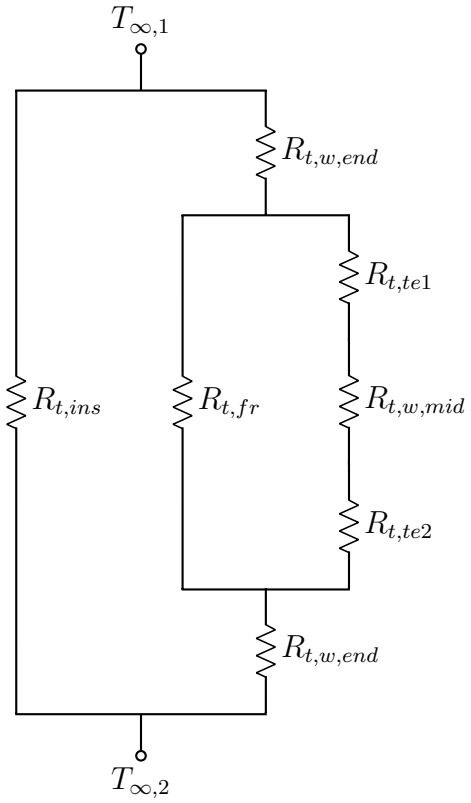

Figure 3-18: Equivalent thermal circuit for split-element numerical simulation case

Another potential solution is to make an assumption about the relationship between c and fringing to reduce the parameter space to two dimensions. Consideration of the system dynamics led to the following assertions:

1. For any combination of g/w and l/g, there exists a value of c that minimizes fringing heat flow.

2. The optimal performance of the device occurs when fringing is minimized.

The effect of these two statements is to fix c at the value which produces the minimum amount of fringing, $c_{fr,min}$, thereby reducing the parameter space to two dimensions.

The validity of the first assertion can be explored by examining numerical simulation results. Similar to the single-element case, a simplified version of the two-element distributed thermal circuit (Fig. 3-18) can be used to find fringing conductance from a known overall conductance, $K_{t,net}$. Recognizing that the thermal resistance is the

same for both elements and the wire ends, the net circuit conductance is found to be:

$$K_{t,net} = K_{t,ins} + \frac{1}{\frac{2}{K_{t,w,end}} + \frac{1}{K_{t,fr} + 1/(2/K_{t,te} + 1/K_{t,w,mid})}}$$

which can be rearranged to yield the fringing conductance:

$$\frac{1}{R_{t,fr}} = K_{t,fr} = \frac{1}{1/(K_{t,net} - K_{t,ins}) - 2/K_{t,w,end}} - \frac{1}{2/K_{t,te} + 1/K_{t,w,mid}} \tag{3.29}$$

$K_{t,fr}$ can again be made non-dimensional via thermal conductivity and element width according to Equation 3.23. Non-dimensional fringing Φ is plotted as a function of c for selected configurations of g/w and l/g in Fig. 3-19. The figure shows that a value of c yielding minimum fringing exists for each configuration. The impact of deviating from the point of minimum fringing also depends on g/w and l/g.

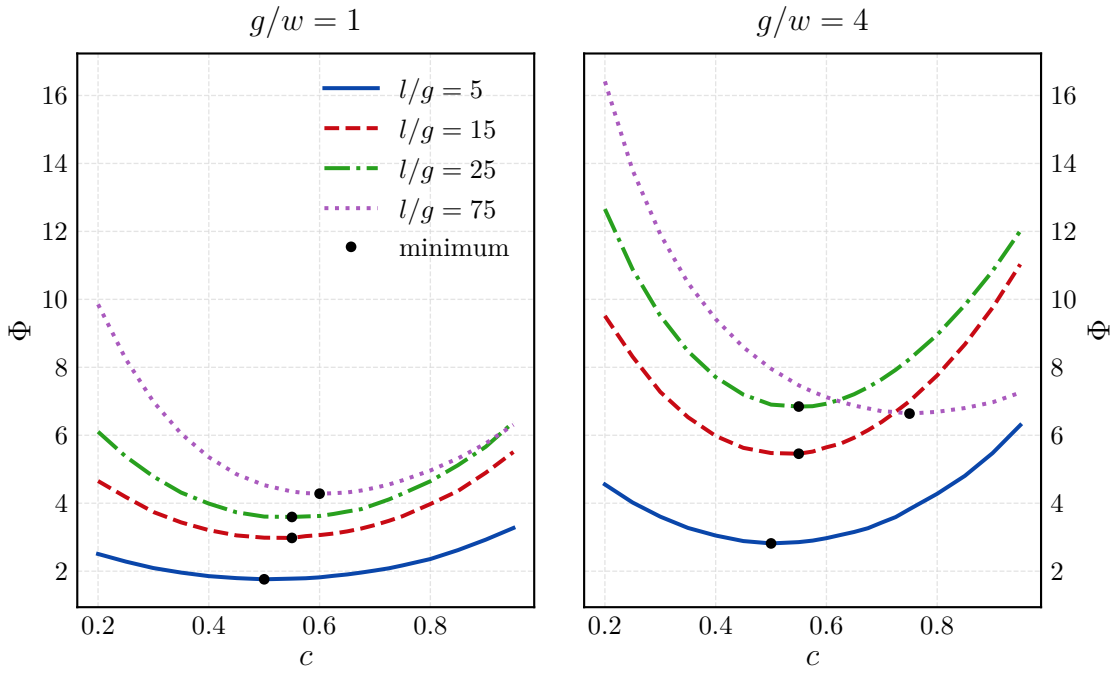

Figure 3-19: Effect of split-element location on fringing

The second assertion holds if the placement of the elements does not affect the physics of the path. If true, c would only affect the fringing heat flow q_{fr}, and the

performance would be optimal where q_{fr} is minimized. Given temperature independent properties, this assertion is nearly true. The sum of the thermal and electrical resistances of the wires, contacts, and elements remains constant even though the individual resistances vary with c. However, the Peltier effect changes asymmetrically; in generation, the decrease in power produced from the top element is not equaled by an increase in power from the bottom element. This effect can be seen in Fig. 3-20, where the relative change in Peltier heat flow γ is defined as:

$$\gamma = \frac{IS_{pn}(T_4 - T_5) - IS_{pn}(T_4 - T_5)_{c=0} - \left[IS_{pn}(T_{11} - T_{12}) - IS_{pn}(T_{11} - T_{12})_{c=0}\right]}{IS_{pn}(T_4 - T_5)_{c=0} + IS_{pn}(T_{11} - T_{12})_{c=0}} \tag{3.30}$$

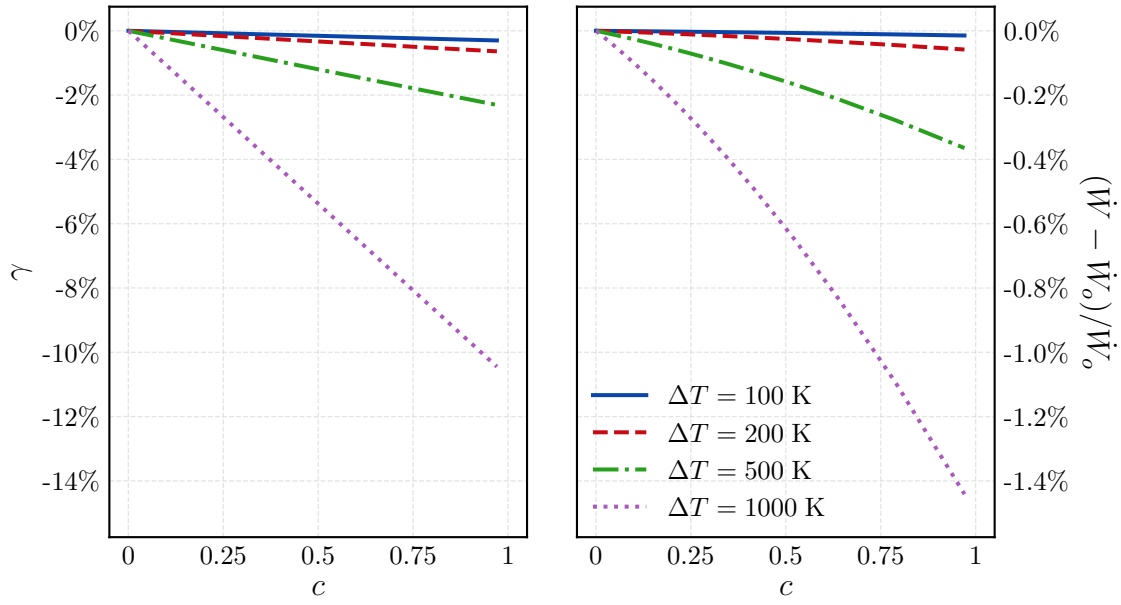

Figure 3-20: Effect of split-element location on Peltier heat flow

The figure shows that this effect exists but has a negligible effect on power output for $\Delta T \leq 200$ and a limited effect up to $\Delta T \leq 500$. In this range, the assumption that c does not affect heat transfer and power generation along the wire path is valid (as is the exclusion of the Peltier effect in the simplified models shown in Figs. 3-9 and 3-18). For $\Delta T \leq 200$, optimal performance is achieved at $c_{fr,min}$. Otherwise, changes in the Peltier effect must be considered when determining element placement.

Having found the assertions to be valid, the parameter space can be reduced to two dimensions by finding $c_{fr,min}$. A large-scale simulation was run for many configurations of g/w and l/g, sweeping over a range of c for each configuration. The value of c that minimized fringing was found, and a basis spline was fit to the data to create a continuous surface. The results and error associated with the fit are shown in Fig. 3-21. Minimum fringing appears to occur when the middle wire length is approximately between 50% to 90% of the total wire length.

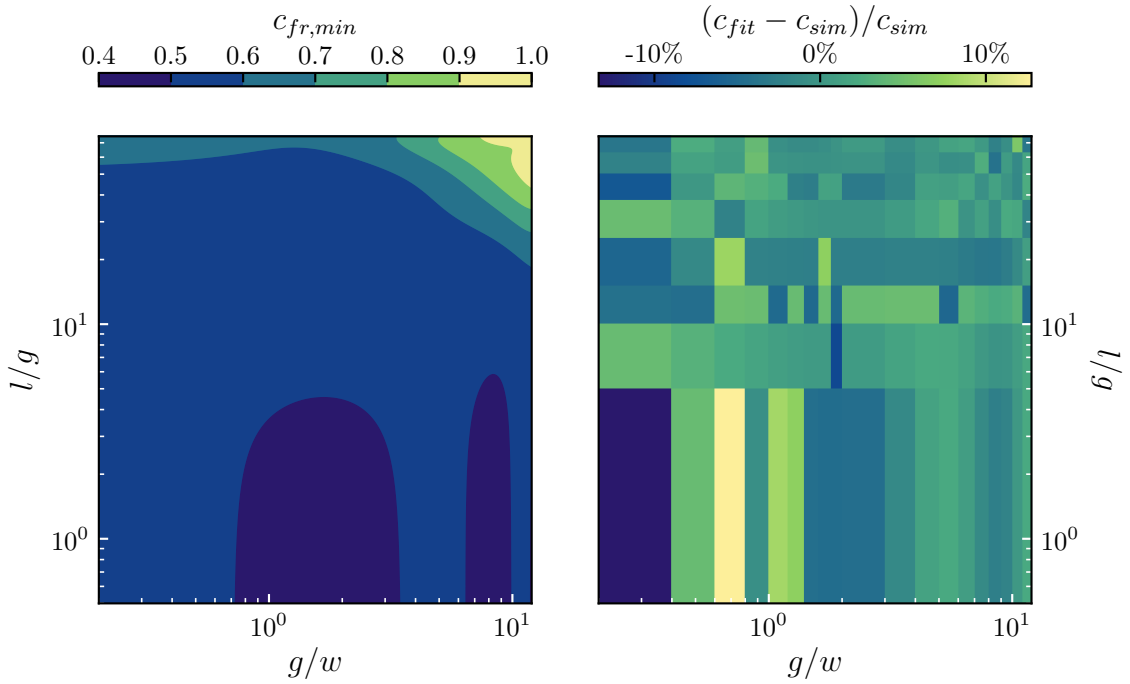

Figure 3-21: Basis spline fit of split-element location for minimum fringing

The corresponding fringing value at the locations of minimum fringing, $\Phi(c_{fr,min})$, was also calculated and fit with a basis spline. Fig. 3-22 shows this fit. The profile is similar to the single-element case (Fig. 3-10) except for large values of g/w, where large l/g values actually decrease split-element fringing. This contrasts with the single-element case where fringing increased with l/g or remained nearly constant for a given g/w.

The most important result is that fringing is significantly less than in the single-element case. From Fig. 3-23, it is evident that splitting the elements can reduce fring-

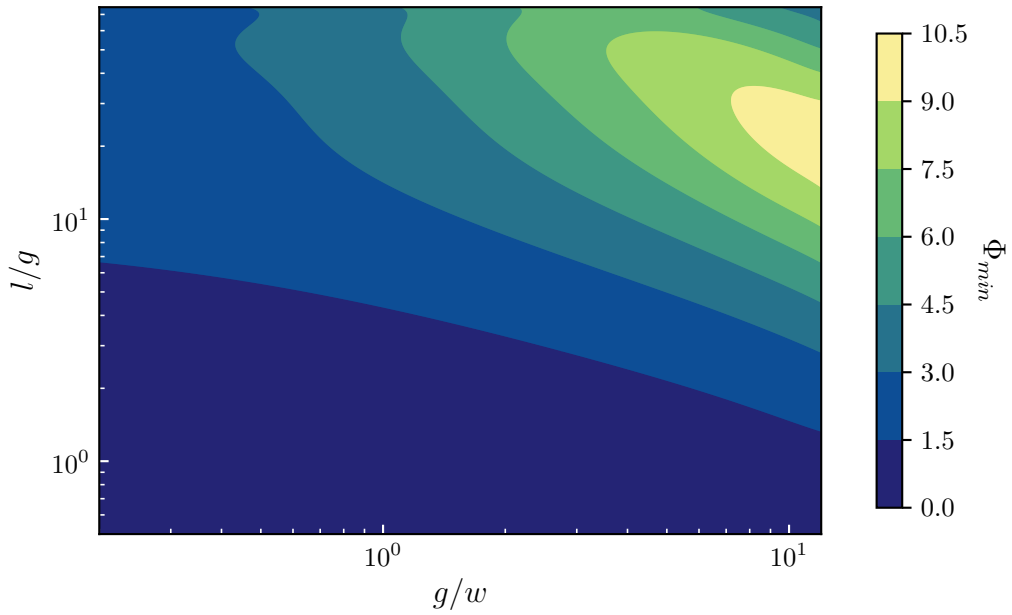

Figure 3-22: Basis spline fit for minimum fringing, split-element geometry

ing from 30% to over 90% depending on the configuration. Should this decrease be sufficient to overcome the added parasitic thermal resistance along the wire, splitting the elements will improve device performance. A summary of this fringing analysis is provided in Table 3.3.

Table 3.3: Summary of fringing results

Configuration	g/w range	l/g range	Φ_{min}	Φ_{max}	maximum error	
					$l/g \leq 5$	$l/g > 5$
Single-Element	0.1 to 12	0.05 to 125	≈ 0	63	$\pm 50\%$	$\pm 20\%$
Split-Element	0.2 to 12	0.5 to 75	0.28	9.5	$\pm 20\%$	$\pm 5\%$

3.4.2 Effects of Domain Width, Split-Element Architecture

It is assumed that splitting the elements does alter the effects of the repeating thermal boundary between the elements. The same exponential decay relationship given in Equation 3.24 and spline fit for rate parameter b are applied to the split-element case.

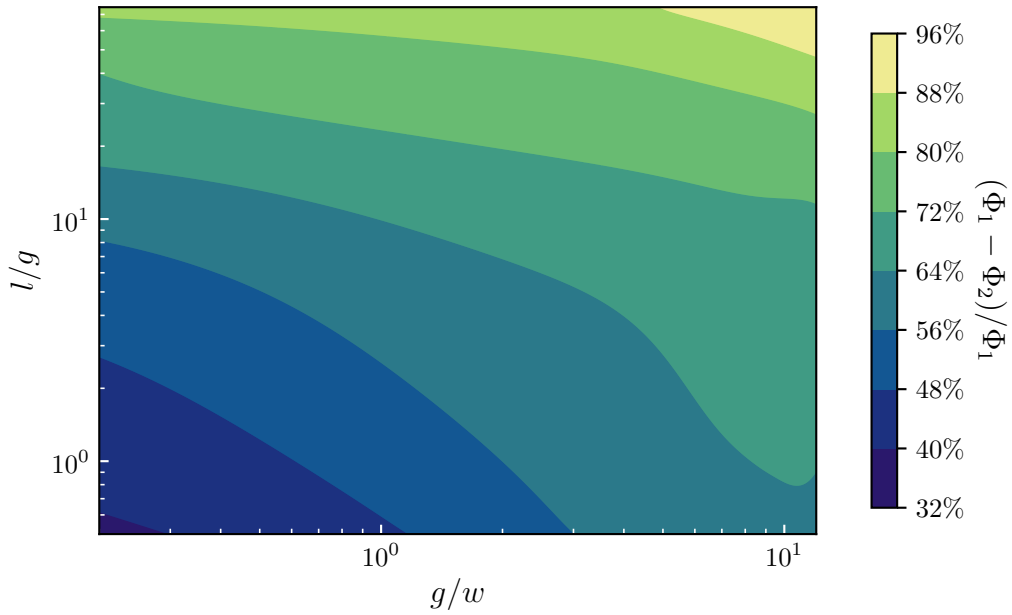

Figure 3-23: Decrease in fringing from single (Φ_1) to split (Φ_2) configuration

3.4.3 Compatibility Factor in the Split-Element Architecture

Although material properties are assumed to be independent of temperature throughout this work, it is worth addressing one issue arising from temperature dependent properties that is relevant to the split-element configuration before continuing. The split-element configuration constitutes a segmented device, where multiple elements of the same type exist along the same current path. Segmentation is usually employed for devices subjected to a large temperature gradient where a single material is only efficient for a portion of the gradient [14]. The behavior of such systems have been explored by Ursell and Snyder [37, 35, 42] and recently have also been studied numerically [29].

In [42], the reduced efficiency for a thermoelectric element η_r, defined as the quotient of overall efficiency and Carnot efficiency, $\eta_r = \eta/\eta_c$, is found to be:

$$\eta_r = \frac{u \cdot \frac{k}{\sigma S}\left(1 - u \cdot \frac{k}{\sigma S}\right)}{u \cdot \frac{k}{\sigma S}\left(1 - u \cdot \frac{k}{\sigma S} \cdot \frac{\Delta T}{2T_H}\right) + \frac{1}{ZT_H}} \tag{3.31}$$

where $u = I/q_{te}$ and $\eta_c = \Delta T/T_H$. In the limit where $\Delta T \ll T_H$, η_r becomes a function of only material properties:

$$\eta_r = \frac{u \cdot \frac{k}{\sigma S}\left(1 - u \cdot \frac{k}{\sigma S}\right)}{u \cdot \frac{k}{\sigma S} + \frac{1}{ZT_H}} \tag{3.32}$$

Finally, the compatibility factor s is derived as the value of u that maximizes η_r:

$$s = \frac{\sqrt{1 + Z\bar{T}} - 1}{S\bar{T}} \tag{3.33}$$

The existence of a maximum u that depends on temperature-dependent material properties must be accounted for when designing a segmented system. Since I is common to the entire system, u may be optimal at s or nearly optimal for one segment but poor for the others. To maximize overall efficiency, the device should be designed so that the compatibility factors of the segments are as similar as possible [37]. This applies to segments of different materials and segments of the same material at different temperatures (self-compatibility) [42].

The split-element distributed architecture introduces some potential flexibility to achieving this goal. Because the properties of each leg are temperature dependent, the compatibility factors of the legs can be tuned by manipulating the dimensions and conductivity of the connecting wire. This adds additional complexity to the determination of the optimal placement of elements and choice of TE materials in the split-element architecture.

This page intentionally left blank.

Chapter 4

Optimization Program

The complexity of the distributed module makes it impractical (though not theoretically impossible) to describe optimal conditions analytically. It is much more useful instead to develop a program capable of both solving the analytic equations presented here and finding optimal solutions for a given parameter space and set of constraints. Using an optimization package provides numerous benefits, including the handling of units, flexibility to set or relax constraints on demand, optimizing for multiple objectives, and multiple modes of operation. The features and their development are discussed here along with some relevant design decisions. The program is validated by simulating existing thermoelectric technologies and comparing results.

4.1 Optimization Framework

The program that models the distributed architecture was built in Python, primarily through the GEKKO Optimization Suite [4]. At its core, GEKKO is an algebraic modeling language (AML) built in Python. An AML solves a problem of the form:

$$\min_{u,x} J(x,u) \tag{4.1}$$

$$0 = f(x,u) \tag{4.2}$$

$$0 \leq g(x,u) \tag{4.3}$$

where the variables x and inputs u are manipulated to minimize the objective function J. While GEKKO specializes in providing extended capabilities for solving dynamic optimization problems (which include differential equations in the objective function and constraint equations), its user-friendly interface and features make it an excellent choice for simply solving steady-state optimization as well. GEKKO leverages Python to give the user intuitive objects and model-building functions and allow the user to choose from many solver configurations. Then, it converts the model to a low-level representation to increase speed. It passes the model to one of the built-in solvers selected by the user, solves the optimization problem, and returns the results back to Python where the user has access to many other powerful packages.

4.1.1 Modes of Operation

At a high level, the distributed module program is designed to provide two basic functions. First, it takes in information about operating conditions from the user, such as exterior temperatures and heat exchange parameters, attached load resistance, or heat to be drawn from the interior of a refrigerator. Then, if a distributed module is specified, the program solves the model and returns the relevant information to the user. Alternatively, the user can specify a range of possible values instead of a specific value, e.g. specifying the element height to be between 1 mm and 5 mm rather than exactly 2 mm. The user will also specify an objective, such as maximizing the power generated by the module. The program will then find a configuration of the variables that achieves this objective.

The GEKKO package includes nine modes of operation, two of which are used to provide the desired functionality. The first of these modes is steady-state simulation. In this mode, GEKKO simply solves for the unknown variables using the provided equations. This requires that the problem is fully constrained, i.e. there are zero degrees of freedom. This mode is used to simulate fully defined configurations from the user. The second mode used is steady-state optimization, in which GEKKO attempts to minimize an objective function of the form given in Equation 4.1. In this mode, the degrees of freedom must be greater than or equal to one.

4.1.2 Solvers

GEKKO includes three built-in, free-to-use solvers: IPOPT [46], an open-source solver (currently maintained by COIN-OR [26]), BPOPT, an interior point solver created by the GEKKO developers, and APOPT [17], a mixed-integer solver also created by the GEKKO developers. The distributed module primarily uses the IPOPT solver, but in some simulation instances better results were achieved with the BPOPT solver, namely in modeling a generation application in Chapter 6.

4.1.3 Generation and Refrigeration

Recall from the discussion in Chapter 1 that the relationship for current differs for generation and refrigeration situations and is specified via known values according to Equation 2.8, 2.11a or 2.11b. GEKKO and Python make this switch simple. In the GEKKO framework, the user specifies which equations are sent to the solver as constraints. The program can toggle between generation and refrigeration models seamlessly with a simple conditional statement:

```
if operation_mode is GENERATION_MODE:
    r_load_tot = r_load * number_np_pairs  # total load resistance
    power = r_load_tot * cur ** 2  # power generated
    r_x1 = number_np_pairs * (q_src - q_snk) == power  # enforce power constraint
elif operation_mode is COOLING_MODE:
    # calculate power - sign changed for consistency elsewhere
    power = -number_np_pairs * (q_src - q_snk)
    # enforce a specified cooling heat load
    r_x1 = q_ex1 * number_np_pairs == heat_load
GEKKO.Equation(r_x1) # add constraint equation to GEKKO object (import not shown)
```

Similarly, the optimization objectives typically differ for generation and refrigeration. For example, a common objective for a generator is to maximize the power output for a given set of conditions, while the equivalent goal for a refrigerator is to minimize the power needed to achieve a desired cooling effect. Again, this distinction can be handled effortlessly:

```
if operation_mode is GENERATION_MODE:
    GEKKO.Obj(-power)  # Minimize -power equivalent to maximizing power
elif operation_mode is COOLING_MODE:
    GEKKO.Obj(power)  # minimize power drawn
```

4.1.4 Single and Split Element Configurations

The single-element and split-element models require some different variable definitions, different fringing spline fits, and a different set of equations. To avoid belaboring the point, suffice it to say that the same techniques used to handle the generator and refrigerator intricacies can adequately address the discrepancies between the single and split element configurations.

4.1.5 Units and Material Properties

To minimize potential bookkeeping errors from manual unit management, a system for managing units was implemented in the distributed module program. The system employs the package Pint, a dictionary of materials, and a unit conversion function to accomplish this goal. Pint [15] allows the user to attach units to numerical quantities, forming *physical quantities*. The user can then perform operations and unit conversions on these physical quantities with either basic Python syntax or other popular packages. Pint quantities can be conveniently created by passing a string containing the desired value and unit as an argument. To leverage this, a script containing materials was built that contains dictionaries for various materials and operating conditions. Each dictionary contains a list of pertinent properties that can be passed to Pint when desired. For example, a thermoelectric material could be indexed as:

```
te_material_1 = dict(
    seebeck_n='-230 uV/K',
    seebeck_p='230 uV/K',
    elec_conductivity_n='104490 1/(ohm*m)',
    elec_conductivity_p='104490 1/(ohm*m)',
    therm_conductivity_n='1.5 W/m/K',
    therm_conductivity_p='1.5 W/m/K',
    mass_density='8098 kg/m**3')
```

When the user wants to run the optimization program, they need only call the thermoelectric material from one of the available dictionaries, and the program will use all the properties when necessary. GEKKO, however, does not support Pint, so all the physical quantities must be returned to numerical quantities before passing them to the solver. Pint makes this process easy as well by providing a method to strip the unit from the numerical value. Here is a simple example of calling a property from the dictionary, assigning it to a variable, converting the unit to the standard SI unit, and stripping its unit for use with GEKKO:

```
import pint
import materials

ureg = pint.UnitRegistry()
te_material = materials.marlow
ntype_elec_conductivity = ureg.Quantity(te_material['elec_conductivity_n'])
ntype_elec_conductivity = ntype_elec_conductivity.to('1/(ohm*m)').magnitude
```

With the Pint package and these techniques, the optimization program handles all unit tasks for the user.

4.2 Modeling Spreading

Adding thermal spreading to the model required some approximation. The relationship for R_s (given in Equation 3.25) contains two infinite sums and an infinite double sum. Obviously, the calculation of infinite sums is impossible in a numerical solver. Calculation of even a moderate number of sums, however, can still dramatically slow the optimization process because the sums must be calculated at each solver step. It is therefore useful to examine the spreading relationship and determine how many terms are required to get sufficiently close to the true value of the spreading resistance.

The spreading resistance relationship depends on the variables given in Table 3.1. The relationship does depend explicitly on each of the variables (save h and k, where it depends on h/k), so the number of terms required will change for different configurations. Here, spreading is calculated for some variable values that are expected

in the distributed module. Namely, $a = 10\,\text{mm}$, $b = 1\,\text{mm}$, $k = 30\,\text{W m}^{-1}\,\text{K}^{-1}$, $h = 5\,\text{W m}^{-2}\,\text{K}^{-1}$, and $t = 2\,\text{mm}$. To visualize the spreading behavior, the dimensions of the larger material section are defined in terms of the smaller material according to the ratio χ, given as:

$$\chi = \frac{a}{c} = \frac{b}{d} \tag{4.4}$$

Fig. 4-1 shows the effect of varying the number of summation terms on the magnitude of R_s. When $\chi \geq 0.04$, the full value of R_s can be calculated with about 20 summation terms, and more than 95% of the value can be calculated with only 9 or 10 terms. When $\chi < 0.04$, the number of terms required begins to increase significantly.

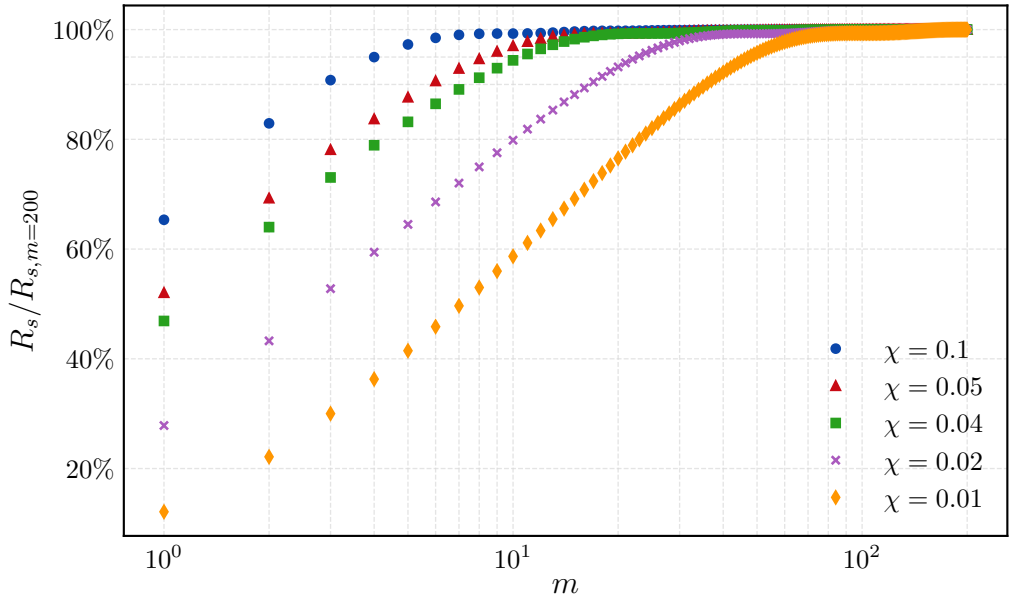

Figure 4-1: Dependency of R_s on number of summation terms ($m = n$)

Needing only 9 or 10 summation terms is clearly computationally desirable to needing 20 or more. It must therefore be determined if $\chi \geq 0.04$ generally for the distributed module. By recognizing that the fill factor is equal to χ^2, the $\chi \geq 0.04$ condition is equivalent to requiring the fill factor be greater than 0.16%. This is a very low fill factor that is likely only optimal for poor external heat exchange coefficients. Thus, it was determined that calculating 10 summation terms is a good starting point as it is sufficient to accurately model spreading resistance for most configurations. If

the optimizer returned a solution with a fill factor less than 1%, the program was set to calculate 20 summation terms and run again to ensure accuracy. On a final note, the ratio h/k also affects the number of terms required. If h is increased from 5 to 5000, about 20 terms are required to reach 95% of true spreading value when $\chi = 0.4$. If instead k is increased, the number of terms required decreases. The number of summation terms should therefore be adjusted if $h \gg k$.

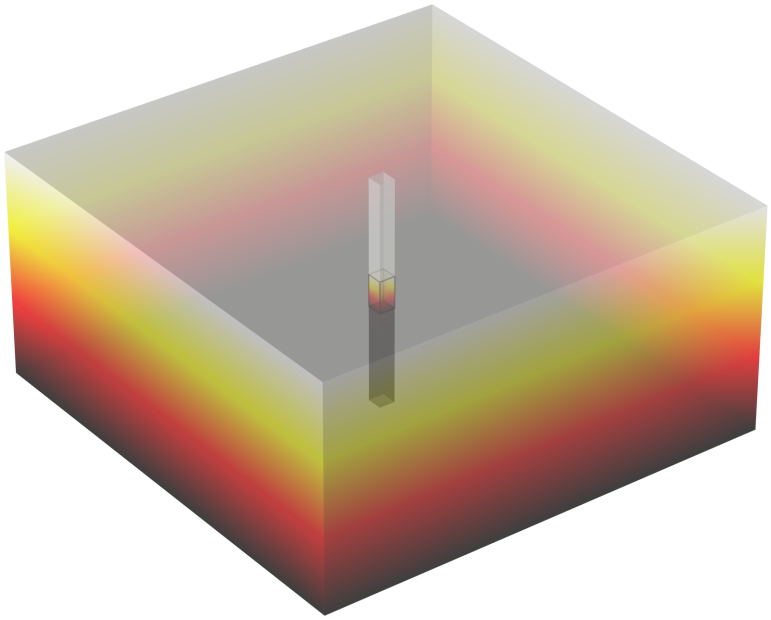

Figure 4-2: Example COMSOL Multiphysics® fringing simulation

4.3 Modeling Fringing

Evidenced by the lengthy explanation in Chapter 3, modeling fringing heat flow was a challenging task. As discussed, numerical simulation results suggested that Roters' method would not be accurate for the distributed architecture model. Fringing would instead be modeled by conducting many numerical simulations and using the results to inform the Python program. Fringing numerical simulations were conducted with COMSOL Multiphysics®. An example geometry is shown in Fig. 4-2. The geometry is a single element connected to two wires. The top and bottom plate temperatures are fixed and a repeating heat flux boundary is enforced on the outer vertical walls of the

geometry. To simplify the geometry and subsequent modeling tasks, the horizontal sections of wire that run along the top and bottom plates are ignored. These wires have relatively high thermal conductivity, large surface area, and small length in the direction of heat flow, so their effects on the overall heat flow are assumed to be minimal. This basic geometry was simulated in parametric sweeps for the pertinent geometric quantities detailed and discussed in Chapter 3.

Having assembled discrete data sets for fringing, spline interpolation was employed to implement this data in the optimization program. GEKKO contains methods for both 1D and 2D basis splines. It uses either raw data or specified spline knots and coefficients to establish a basis spline in the solver's framework and connect the independent and dependent variables. For the distributed module, a function was created using the SciPy package [45] to determine basis spline knots and coefficients from processed COMSOL Multiphysics® data. This was done so that the splines could be checked for over-fitting issues or poor conditioning on the data. Once satisfied with the fit, the spline information was then applied in the GEKKO methods. A simple example below illustrates the ease of creating and implementing such splines. NumPy [43], used liberally throughout the program, is also employed here.

```
m = gekko.GEKKO()  # create gekko object

# find B-spline knots and coefficients (kx, ky set degree)
tck = scipy.interpolate.bisplrep(x=ar_grid, y=lr_grid, z=K_fr_nd_data, kx=5, ky=5)

# create variables in gekko object
aspect_ratio = m.Var(value=1, lb=numpy.min(ar_grid), ub=numpy.max(ar_grid))
len_ratio = m.Var(value=1, lb=numpy.min(lr_grid), ub=numpy.max(lr_grid))
K_fr_nd = m.Var(value=20, lb=0)

# link gekko variables using SciPy B-spline
m.bspline(x=aspect_ratio, y=len_ratio, z=K_fr_nd, x_data=tck[0], ydata=tck[1],
          z_data=tck[2], data=False, kx=tck[3], ky=tck[4])

# relate geometric ratios to dimensions
r_g1 = aspect_ratio == te_length / te_width
r_g2 = len_ratio == (2 * wire_l_out) / te_length  # for one-stage architecture
m.Equations([r_g1, r_g2])
```

4.4 Objective Function Flexibility

A final notable feature is the ability to customize the optimization goal. Should additional dimensions be added to the model (e.g. cost, weight), the program can easily be modified to include these dimensions in the optimization analysis. Alternatively, they can be used as constraints for other optimization objectives. And, incorporating additional dimensions is as simple as including relevant variables and equations and adding pertinent material properties to the dictionaries. Below are just a few examples of how the objective can be manipulated for generation and refrigeration. Clearly, the possibilities for program expansion are numerous.

```
# generation objectives
m.Obj(-power)  # maximize power generated

m.Obj(-power / q_src)  # maximize efficiency

m.Equation(power ⩾ power_min)  # specify a minimum power required
m.Obj(cost / power)  # minimize $/W subject to minimum power, cost function

m.Equation(mass ⩽ mass_max)  # specify maximum allowable mass
m.Obj(-power)  # maximize power generated subject to mass constraint
----
# refrigeration objectives
m.Obj(power)  # minimize power draw

m.Obj(-q_src / power)  # maximize coefficient of performance

m.Equation(power ⩽ power_max)  # specify a maximum allowable power draw
m.Obj(cost)  # minimize total cost subject to maximum power draw, cost function

m.Equation(mass ⩽ mass_max)  # specify maximum allowable mass
m.Obj(-q_src / power)  # maximize COP subject to mass constraint
```

4.5 Program Validation

It is necessary to test the optimization program and determine its validity. Because distributed modules have not yet been built extensively, validating the model is currently limited to theoretical tests and comparison to existing thermoelectric devices. Some intuitive theoretical tests were employed to validate behavior, including:

- Determining whether or not heat is flowing in the expected direction
- Determining whether or not relative heat flow magnitudes are reasonable
- Observing if the program drives towards limiting boundary conditions, and if such behavior makes sense given the input conditions
- Ensuring changes in material properties or input conditions affect performance attributes as expected
- Evaluating optimality by simulating neighboring configurations

These types of checks are conducted both through pytest [23] and manual user observation of solver results. In addition, the solver outputs error codes for each solution, which tell the user if a solution was successfully found or what type of problem the solver encountered. These codes provide a starting point for troubleshooting solutions. Once solutions are successful, the aforementioned tests can be implemented.

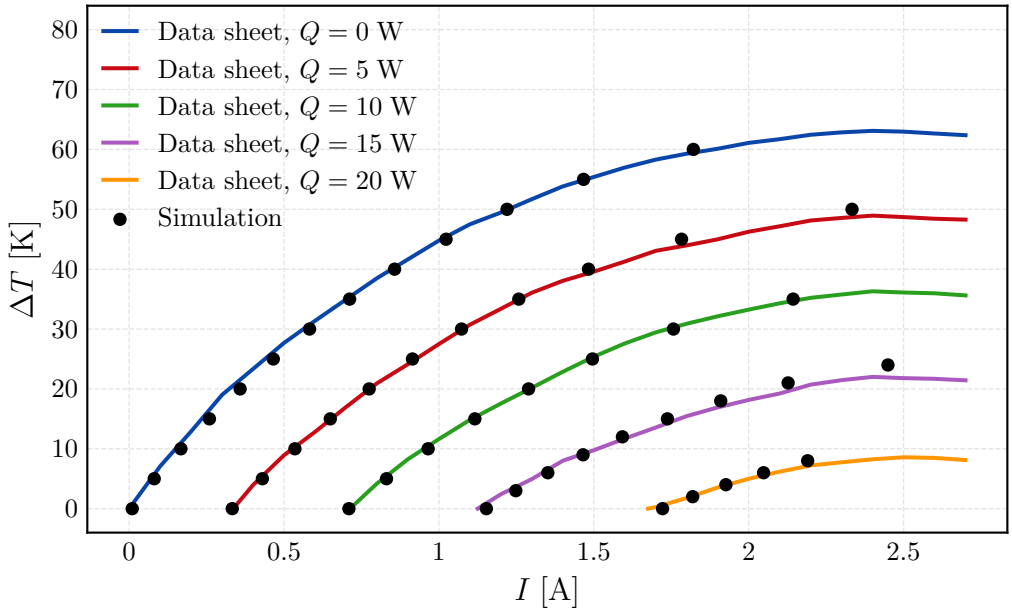

Figure 4-3: RC12-2.5 refrigeration performance comparison

In addition to theoretical validation, the model can be compared to existing thermoelectric devices with available experimental data. Though parts of the model are

insignificant when modeling traditional devices (e.g. spreading resistance and fringing) and therefore not truly tested, simulation of traditional devices can at least provide validation of the general effectiveness of the program. Here, the model is validated against the RC12-2.5 device developed by II-VI Marlow, Inc. The RC12-2.5 data sheet [18] provides performance curves for both refrigeration and generation performance. The specified operating conditions and device dimensions were simulated with the modeling program. Fig. 4-3 shows reported and simulated refrigeration performance for various applied heat loads. The simulation results closely match the reported performance, though some error is present for larger heat loads. Similarly, Fig. 4-4 shows reported and simulated generator performance. The simulation results match the data sheet with minimal error.

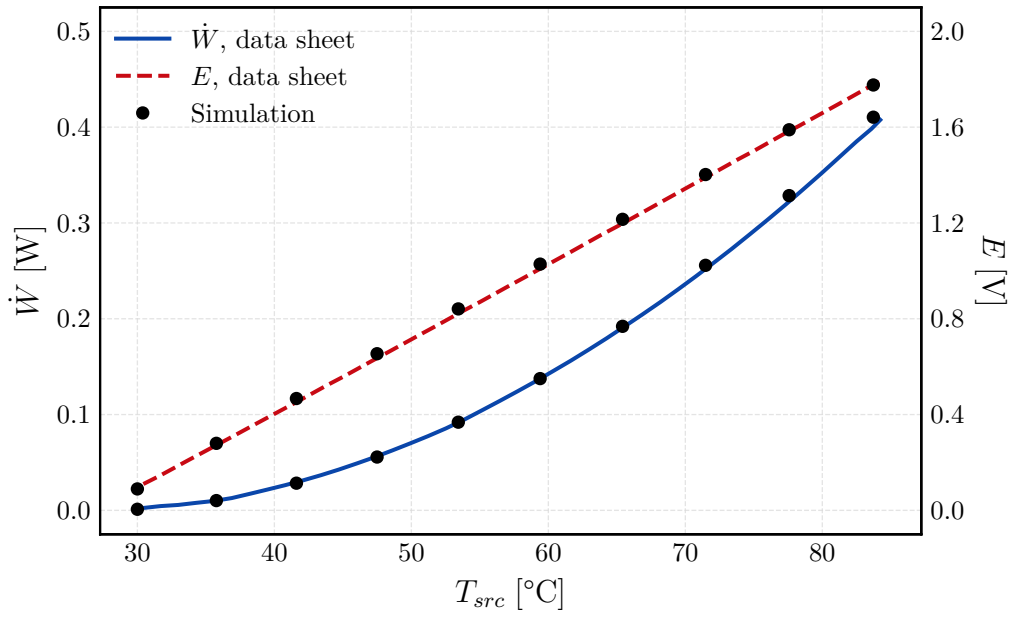

Figure 4-4: RC12-2.5 generation performance comparison ($T_{snk} = 27\,°\text{C}$)

This page intentionally left blank.

Chapter 5

General Performance

The modeling program developed in the previous chapter enables evaluation and comparison of distributed architecture performance. The purpose of this chapter is not to attempt to portray performance in every possible scenario. Such a task would be difficult and require a long-winded explanation due to the wide-ranging and multi-dimensional design space. Instead, a subset of conditions will be explored and compared to the traditional architecture with the goal of highlighting interesting and useful relationships.

The primary design concepts explored here are those presented in previous chapters, namely fill factor, the de-coupling of device and element dimensions, and parasitic losses introduced by the distributed architecture. The effects of each of these are evaluated through the developed program's simulation and optimization tools. Operating conditions, parameters, and performance metrics differ for generation and refrigeration; setup, results, and analysis discussions are therefore grouped accordingly. Finally, some common observations and conclusions are presented.

Generally, the analysis is structured as follows. First, a traditional architecture is simulated for a selected range of conditions. A distributed architecture is then optimized for the same range of conditions and element dimensions. The behavior is explored to show the impacts of the distributed architecture employing existing thermoelectric elements. Following this, variable element and split-element optimizations are also conducted and evaluated.

5.1 Generation

The generation optimizations and simulations are designed to explore dependencies on the overall heat exchange coefficient U, which varies over three orders of magnitude. Relevant parameters are given in Table 5.1, and material properties can be found in Table A.1. The parameters for the traditional TEG simulation are given in the *value* column and the parameter boundaries for the distributed TEG optimization are given in the remaining columns. Any entry without boundaries is defined as a constant for the optimization. To create a point of comparison, the overall device area is fixed at $100\,\mathrm{cm}^2$ for both traditional and distributed TEGs.

The optimization and simulation results are displayed in Fig. 5-1, where the distributed TEG was optimized for maximum power output. The results indicate that the distributed TEG can produce equivalent or greater power at every value of U. The optimal fill factor is found to be less than the traditional fill factor for $U \lesssim 750\,\mathrm{W\,m^{-2}\,K^{-1}}$. The optimal TEG thickness h_{mod} and efficiency η are also greater than the traditional TEG values in this range.

The results support previous assertions. When heat exchange to the environment is poor, decreasing the fill factor increases the area available to the TE elements for heat exchange and power output. In conjunction, the device height is increased to prevent a thermal short from occurring through the insulation between elements. Conversely, when heat exchange conditions are favorable ($U \gtrsim 1000\,\mathrm{W\,m^{-2}\,K^{-1}}$), the optimal fill factor increases and the device height decreases to its lower limit. The traditional TEG design appears to be optimal only for a singular condition.

At a high level, the results suggest that a distributed TEG could better meet generation demands in many applications. For scenarios with relatively low heat exchange coefficients, a distributed TEG could produce a required amount of power with less thermoelectric material. In some scenarios, a distributed TEG may improve efficiency enough to permit the use of a cheaper, less effective heat exchanger - or even no heat exchanger at all. The increased thickness of the device is also likely to reduce thermo-mechanical stress and improve durability.

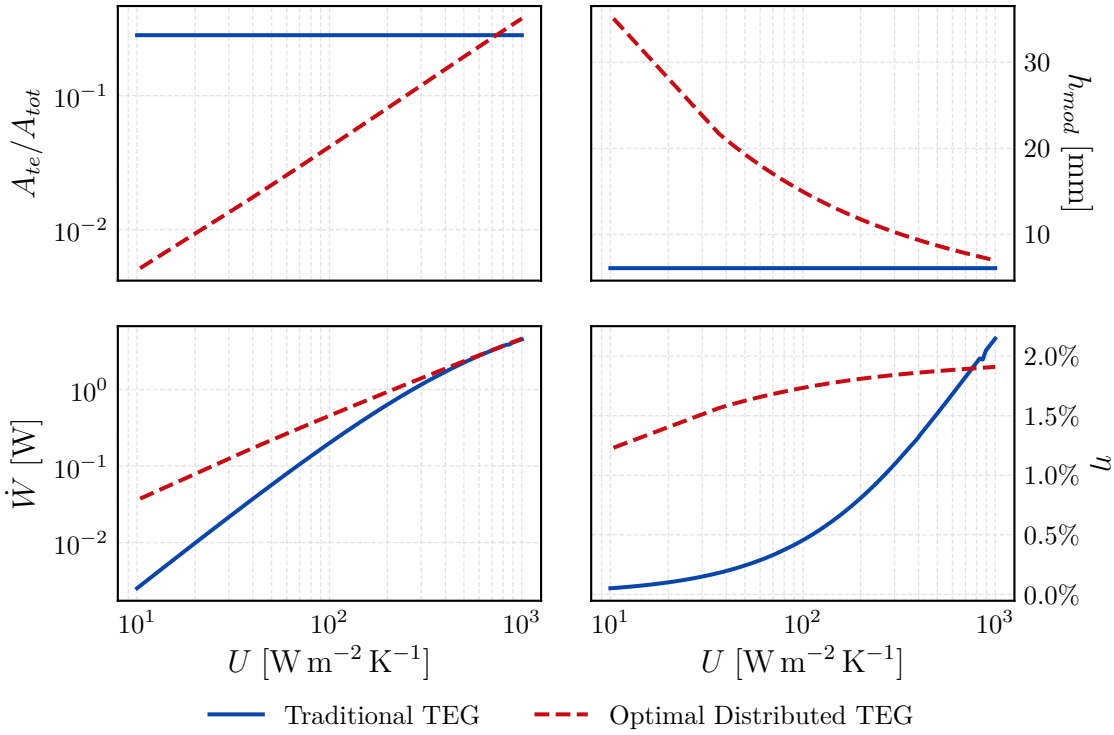

Figure 5-1: Comparison of generator performance, $\Delta T = 100\,\mathrm{K}$

Table 5.1: Selected parameters for generation simulation and optimization

Parameter	Value (Traditional)	Lower Bound	Upper Bound
TE element area	$1.0\,\mathrm{mm}^2$		
TE element length	$2.0\,\mathrm{mm}$		
Plate thickness	$2.0\,\mathrm{mm}$		
Device height	$6.3\,\mathrm{mm}$	$6.3\,\mathrm{mm}$	$10\,\mathrm{cm}$
Device area	$100\,\mathrm{cm}^2$		
Number of n-p pairs	1411	1	∞
Fill factor	0.28	0	0.99
TE element spacing	$0.88\,\mathrm{mm}$	$100\,\mu\mathrm{m}$	
$R_{e,load}$	$R_{e,internal}$		
	Range		
$U_{src} = U_{snk}$	1 to 1000 $\mathrm{W\,m^{-2}\,K^{-1}}$		

A similar optimization was conducted with variable thermoelectric element dimensions. The constraints and results of the optimization are given in Table 5.2 and Fig. 5-2, respectively. The optimal distributed design from Fig. 5-1 is also shown for comparison. For much of the range of U, the optimal element aspect ratio (l_{te}/w_{te}) is greater than the fixed 2:1 ratio defined in the previous optimization. The greater aspect ratio reduces the fringing heat flow and heat flow through the insulation. The result is improved TEG efficiency, particularly at lower U values. At high U values, the element width appears to increase dramatically, but this only occurs to increase the fill factor after the minimum allowed element spacing has been reached.

Table 5.2: Variable element simulation parameters

Parameter	Value (Traditional)	Lower Bound	Upper Bound
TE element area	$1.0\,\mathrm{mm}^2$	$0.01\,\mathrm{mm}^2$	$100\,\mathrm{mm}^2$
TE element length	$2.0\,\mathrm{mm}$	$0.1\,\mathrm{mm}$	$10\,\mathrm{mm}$

Although the variable-element optimized TEG performs better, it may not be practical in every situation. At its largest, the TEG is about 7 cm thick and three times as thick as the comparable distributed TEG. It also uses more thermoelectric material, significantly so in many cases.

Alternatively, a split-element configuration could also improve performance by reducing fringing. Fig. 5-3 shows the performance for split-element configurations with fixed and variable element geometries. For fixed elements, the optimal split configuration significantly reduces fringing while slightly increasing the device height and maintaining a similar fill factor. For low U values, the split configuration improves efficiency, but as U increases, the efficiency gains from reduced fringing are outweighed by the additional contact resistances in the split-element configuration. For a variable element scenario, splitting the elements has minimal effect as fringing is minimal to begin with. Although these effects are important, it must be remembered that the primary advantage of the split-element architecture is the ability to segment materials and tune compatibility factors with element placement (see Section 3.4.3).

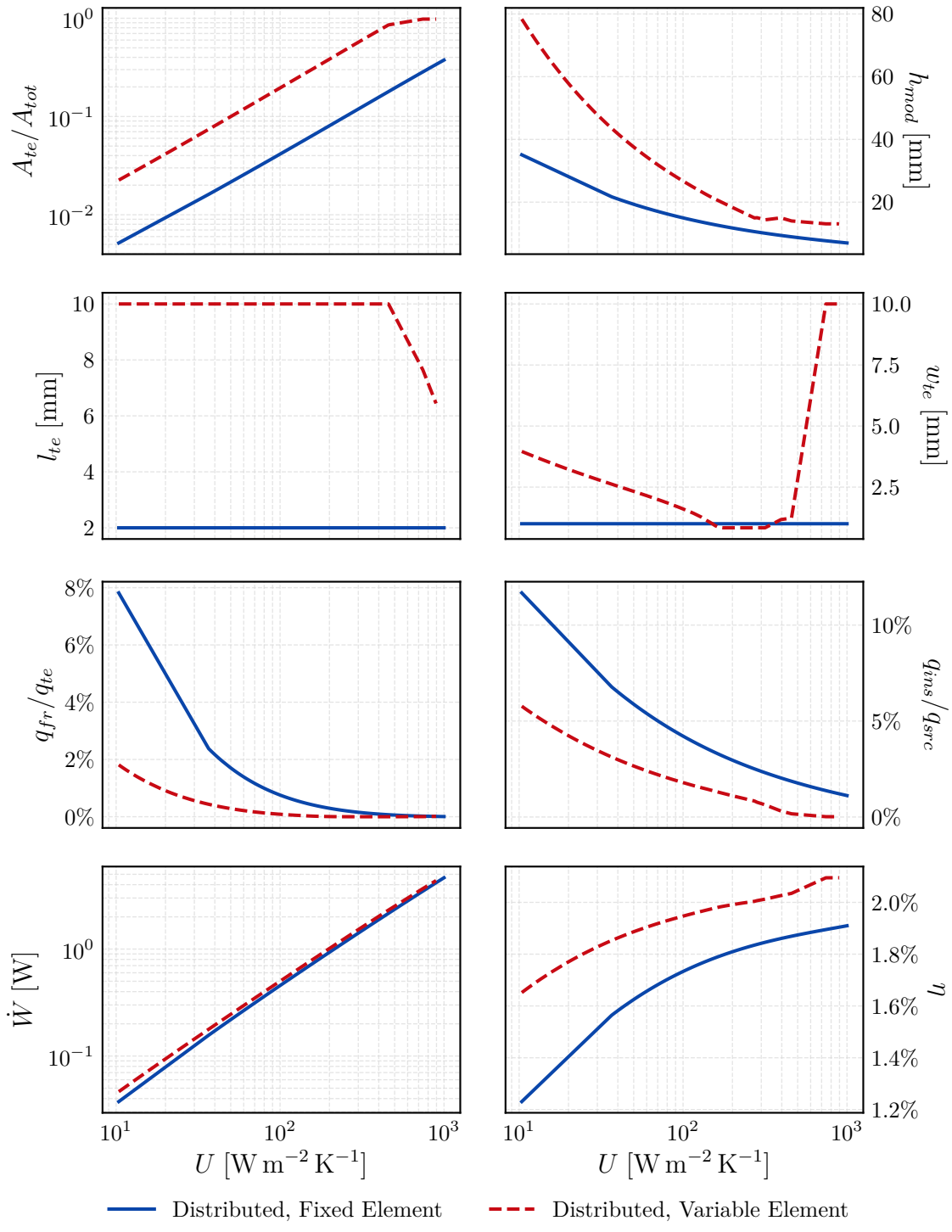

Figure 5-2: Generator performance with variable element dimensions

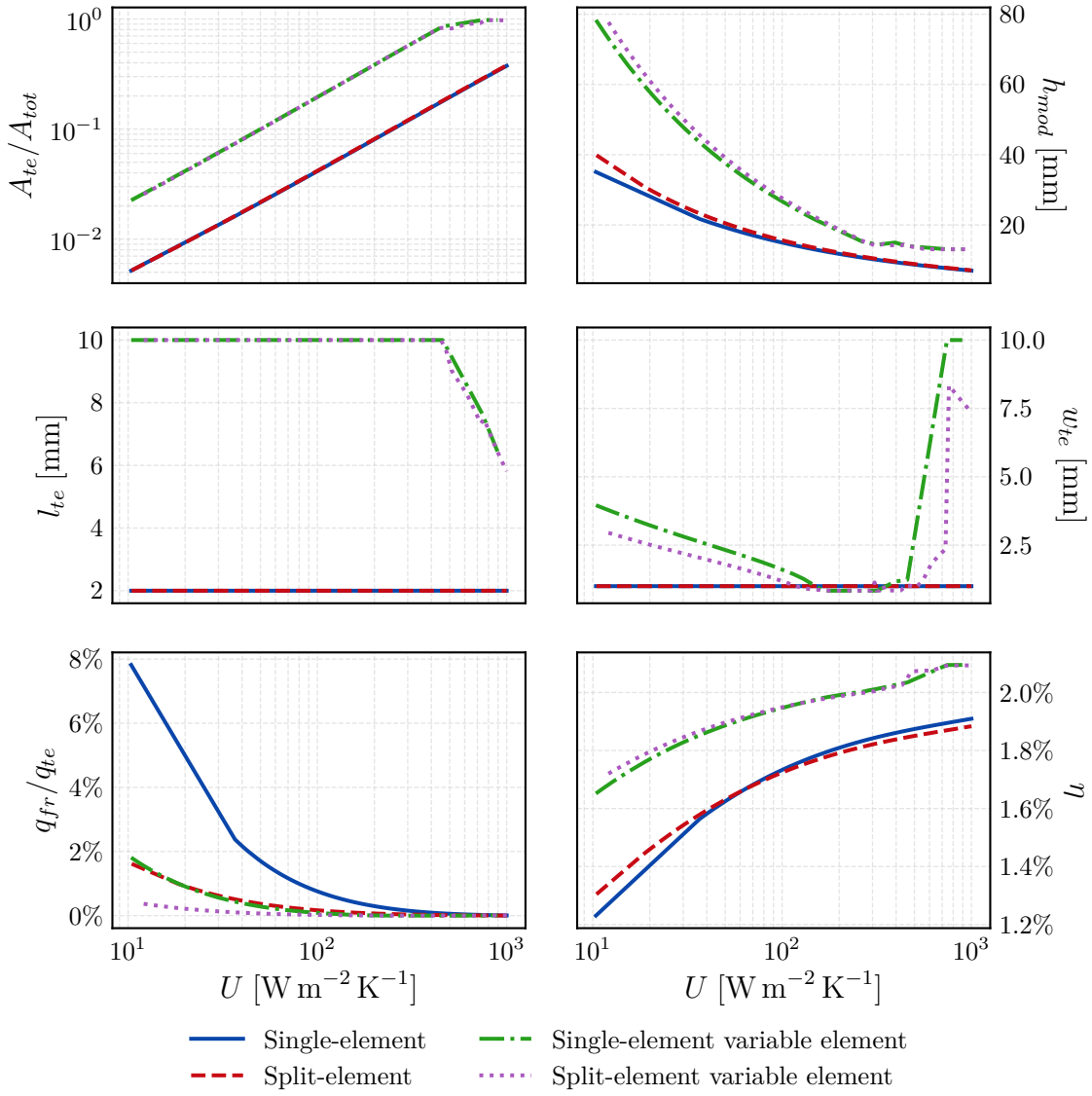

Figure 5-3: Split-element generation performance

5.2 Refrigeration

The refrigeration studies consider the effects of applied heat load q_{src} and external heat exchange coefficient U on the architectures. Parameters are given in Table 5.3 in the same manner as before. The temperature gradient between the source and the sink was set to zero throughout for simplicity, as an applied temperature gradient is effectively an additional heat load. It is assumed that heat exchange on the interior of the refrigerator is excellent and that U applies only to the exterior. Again, the overall size of the device is fixed, but the number of thermoelectric pairs may vary for the distributed architecture.

The distributed architecture was optimized to minimize the power required to draw the applied heat load. Because the heat load is specified and fixed, this is equivalent to maximizing the coefficient of performance ϕ. The performance of both architectures are shown in Fig. 5-4. The distributed architecture again improves performance. For all three heat exchange conditions shown, the distributed architecture yields a better coefficient of performance than the traditional architecture. It also increases the maximum amount of heat that can be pumped from the source: where $U = 50\,\mathrm{W\,m^{-2}\,K^{-1}}$ and $100\,\mathrm{W\,m^{-2}\,K^{-1}}$, the traditional device is only able to pump up to approximately 1 W and 3 W while the distributed devices pump a maximum of 2 W and 7 W, respectively.

The themes discussed in the previous section are again evident here. Under relatively poor heat exchange conditions, optimal device fill factor is less than the traditional design. Although the current draw is increased in these configurations, the reduction in the amount of pairs still renders an improvement to ϕ. To avoid thermal shorting through the insulation, the device height is increased. Overall, the results again show that the distributed architecture can improve performance for a wide range of operating conditions. The improved efficiency of the distributed TEC could reduce the amount of thermoelectric material needed to achieve the targeted cooling performance. It may also allow the use of a cheaper heat exchanger or eliminate the need for one entirely.

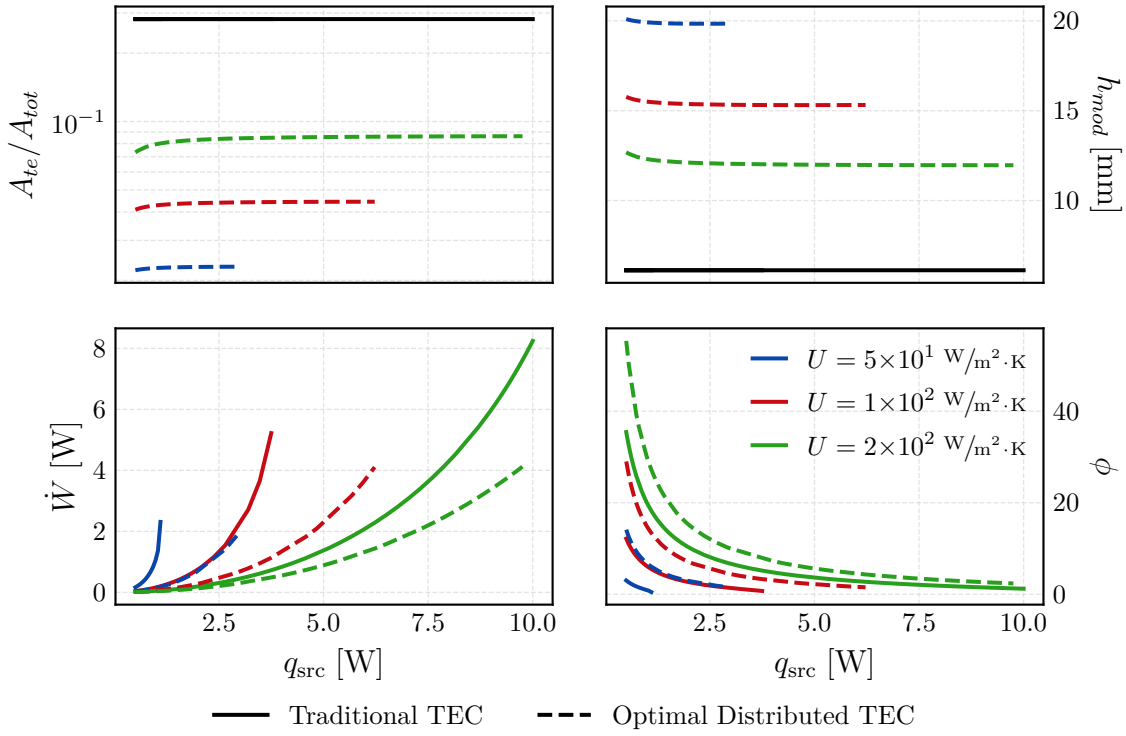

Figure 5-4: Comparison of refrigerator performance, $\Delta T = 0\,\text{K}$

Table 5.3: Selected parameters for refrigeration simulation and optimization

Parameter	Value (Traditional)	Lower Bound	Upper Bound
TE element area	$1.0\,\text{mm}^2$		
TE element length	$2.0\,\text{mm}$		
Plate thickness	$2.0\,\text{mm}$		
Device height	$6.3\,\text{mm}$	$6.3\,\text{mm}$	$10\,\text{cm}$
Device area	$100\,\text{cm}^2$		
Number of n-p pairs	1411	1	∞
Fill factor	0.28	0	0.99
TE element spacing	$0.88\,\text{mm}$	$100\,\mu\text{m}$	
U_{src}	∞		
	Range		
U_{snk}	50, 100 and $200\,\text{W}\,\text{m}^{-2}\,\text{K}^{-1}$		
q_{src}	0.5 to $10\,\text{W}$		

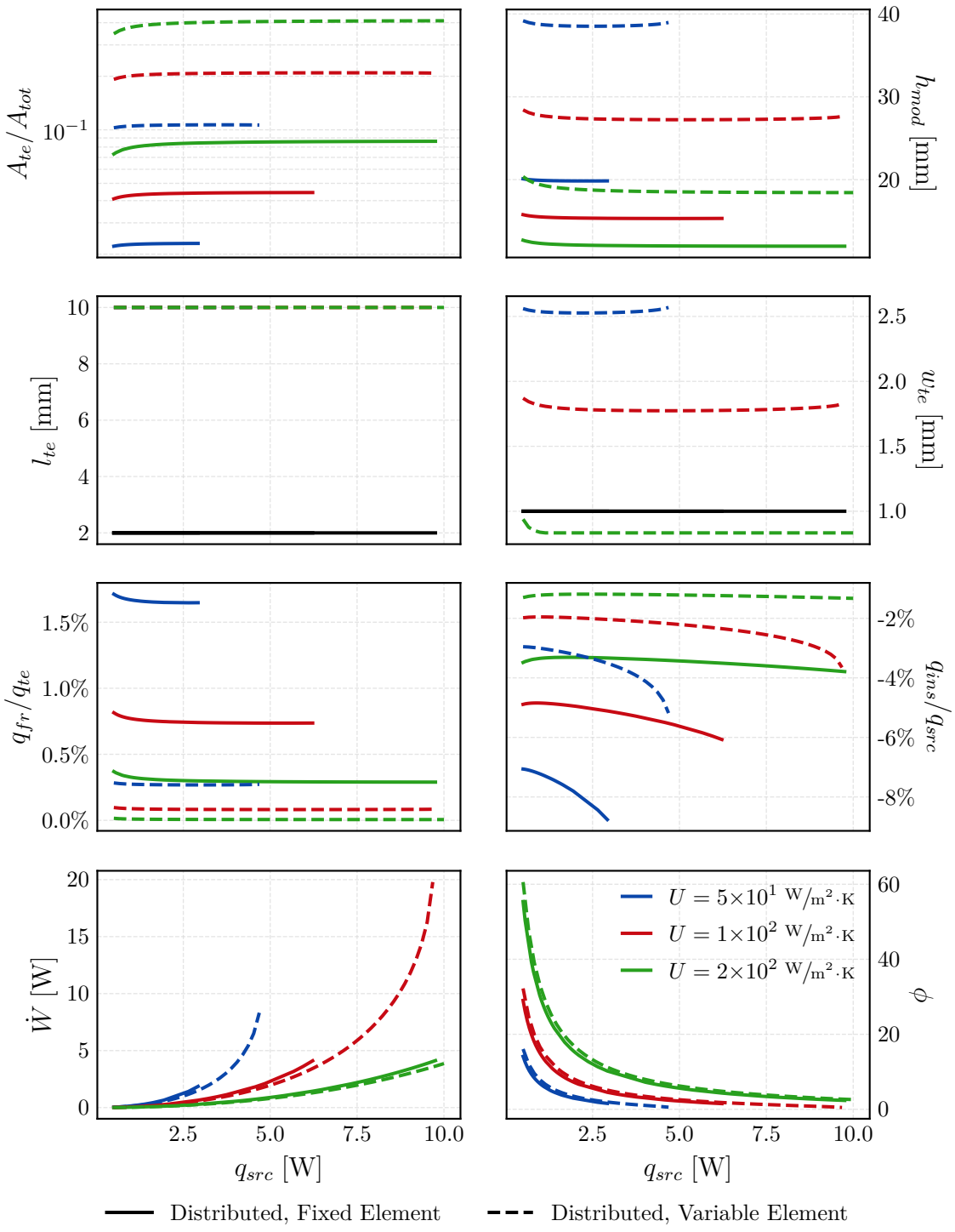

Figure 5-5: Refrigerator performance with variable element dimensions

Again, an optimization was conducted with variable element dimensions according to Table 5.2. The resultant performance is shown in Fig. 5-5 along with the fixed-variable performance for comparison. Like generation, the optimal element aspect ratio (l_{te}/w_{te}) is greater than 2:1 (and increases with U) resulting in reduced fringing. The optimal thickness and fill factor are also greater throughout. This results in less fringing around the element and leakage through the insulation. Overall, the maximum heat pumping capacity and coefficient of performance are increased.

Optimal split-element configuration performance is shown in Fig. 5-6. Unlike generation, the split-element configuration appears to have minimal impact on device performance. While splitting the elements reduces fringing as expected, the fringing heat flow is already low due to the small temperature gradients present. The decrease in fringing therefore does not translate into significant performance improvements, but it does slightly increase the maximum heat that can be drawn from the source in low U scenarios. In systems with greater temperatures gradients, fringing would become more important and the split-element architecture may provide greater benefits similar to those seen in generation.

5.3 Common Observations

Some common themes emerged from the generation and refrigeration studies. In both applications, the distributed architecture performed similar to or better than its traditional counterpart, most notably for low values of U. The improvements from the distributed architecture may enable a device to achieve desired performance without an attached heat exchanger. The observed performance improvement can largely be attributed to proper matching of fill factor and device thickness to the conditions. The optimization of element dimensions improved performance further, although its implementation may be impractical in situations where space is limited. Split-element designs may also be used, particularly when compatibility factor is of concern. In short, the distributed architecture introduces new parameters that may be manipulated to bring performance closer to the theoretical maximum set by ZT.

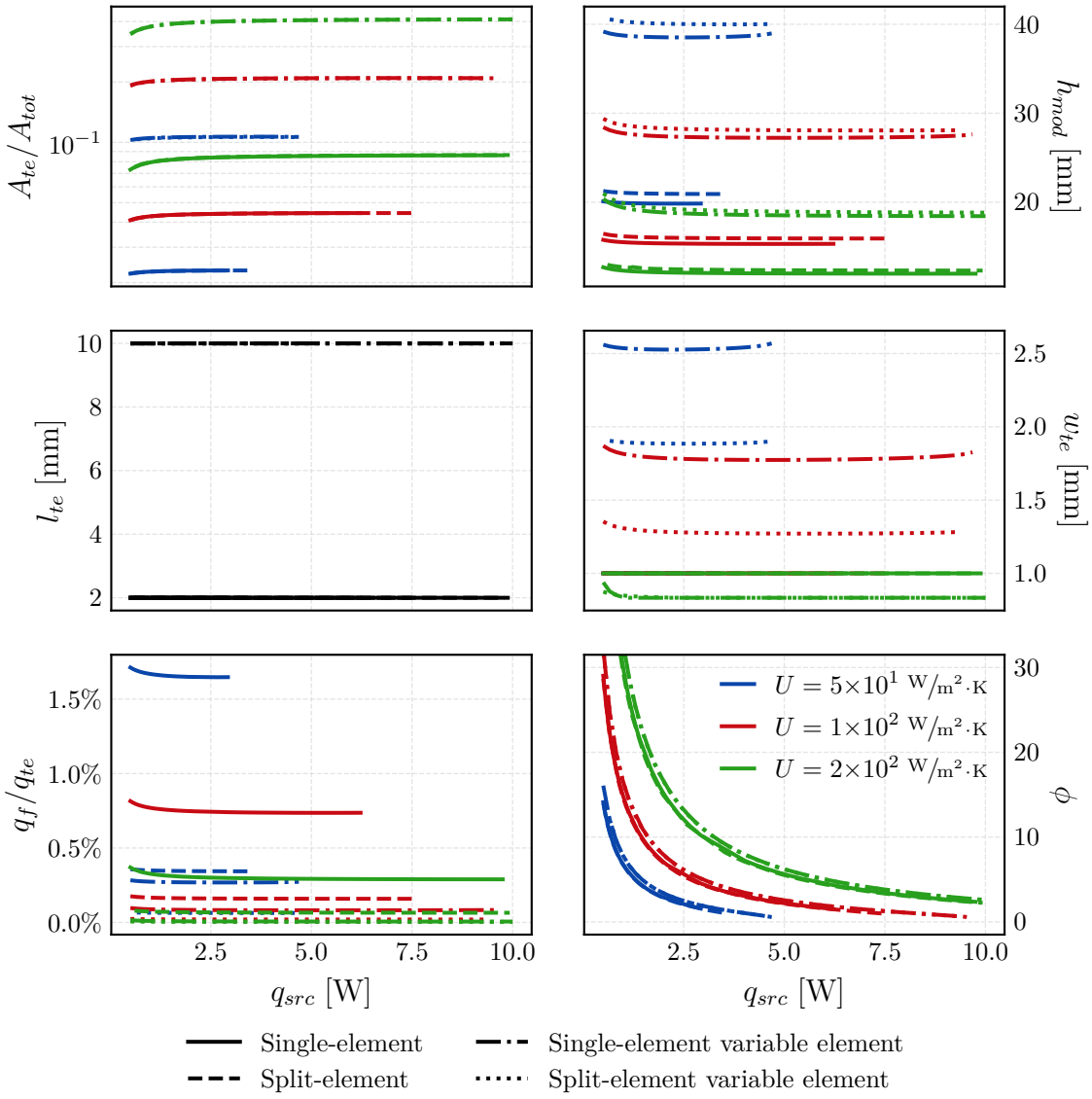

Figure 5-6: Split-element refrigeration performance

This page intentionally left blank.

Chapter 6

Application: Aircraft Sensor Power

With the general behavior of the distributed architecture understood, a specific application is now considered to further illustrate its advantages. Recently, there has been interest in utilizing thermoelectric generators to power wireless sensors in aircraft [2, 34, 44]. A major goal for aircraft maintenance is to predict potential causes of failure before they occur and thereby prevent more costly issues from arising [8]. This is particularly true for the aircraft structure, where identifying and remedying corrosion and cracks is essential. Structural Health Monitoring (SHM) systems routinely employ sensors to collect data that aides in monitoring structural integrity. Traditionally, wired sensors are used, but the long lengths of wire required add weight to the aircraft and make assembly complex [9]. A network of wireless sensors has been found to be potentially advantageous because it would solve these weight and assembly issues and could reduce maintenance costs [8].

Such wireless sensors require a lightweight, reliable power source. Batteries could effectively supply the necessary power but are undesirable because they require charging or replacement [9], both of which are difficult for sensors placed in hard-to-reach areas of the aircraft. Thus, an energy harvesting generator (or a combination of generators) is desirable and has been described in depth [44].

One potential energy available for harvesting is the thermal gradient that occurs during aircraft takeoff and landing, which could be captured using a thermoelectric generator [44]. Throughout the flight, thermal gradients fluctuate from negligible

to useful for significant energy generation. A novel thermoelectric system has been introduced that leverages these fluctuations to provide consistent energy. The design utilizes a phase-change material (PCM) to create a temperature gradient across the thermoelectric device and generate power. Excess produced energy is then stored for later use when the exterior temperature gradient is not significant. PCM TEGs are theorized, modeled, and experimented with in [21, 22, 33, 34]. An overview of the theoretical background presented in [22] follows here.

6.1 Thermoelectric Generation with PCM

A simple phase-change material thermoelectric generator (PCM TEG) based on the design presented in [22] is shown in Fig. 6-1, and an annotated cross section is shown in Fig. 6-2. The TEG is fixed between the exterior skin of an aircraft wing and a chamber containing the PCM. The chamber contains thermal bridges to help circulate heat throughout the PCM and is insulated to prevent heat leakage. The TEG produces power when a temperature gradient exists between the external ambient air and the PCM.

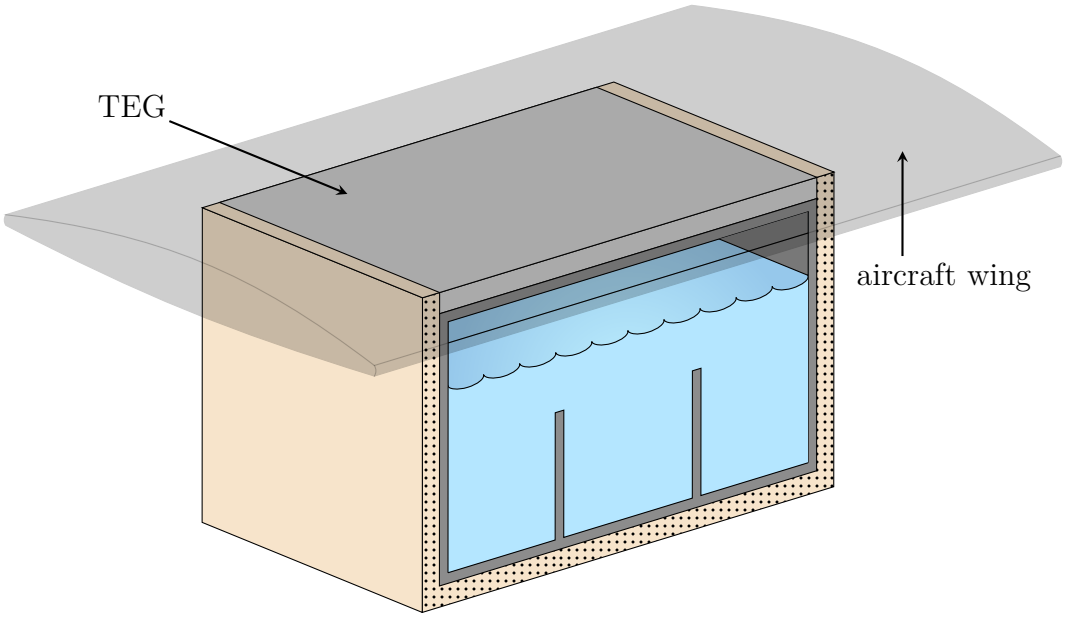

Figure 6-1: PCM thermoelectric generator attached to aircraft wing

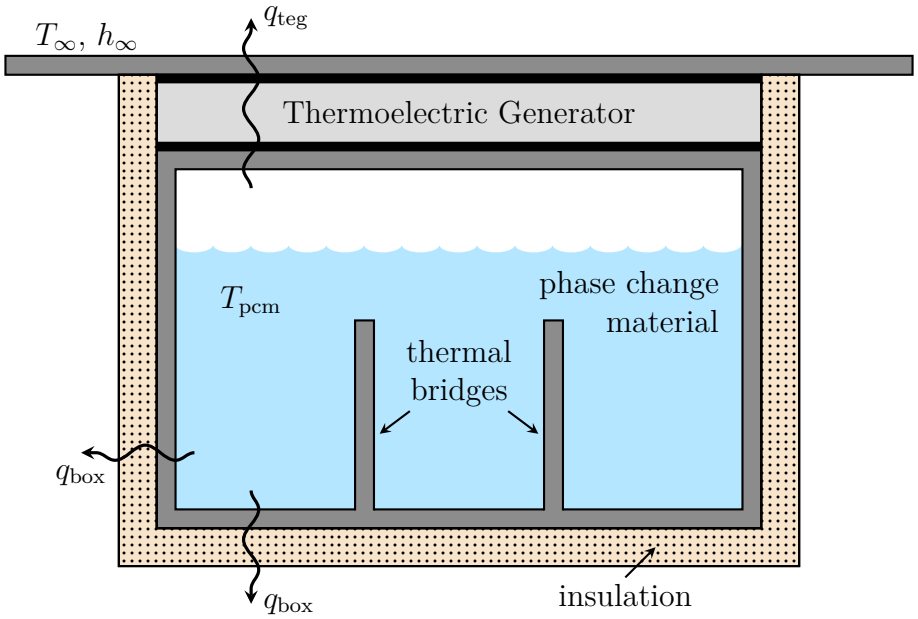

Figure 6-2: Annotated cross-section of PCM TEG

The primary modeling difference between the PCM TEG and the traditional TEG situation is the introduction of variable external source and sink temperatures. The external sink temperature – the ambient temperature surrounding the aircraft wing – is a measurable and known quantity. The interior temperature depends on the energy present in the PCM. In addition to the previous theoretical assumptions made, it is assumed here that the PCM and its surrounding chamber are of a uniform temperature and that the PCM is the sole contributor to stored heat energy.

6.1.1 Discrete-Time Modeling

The change in internal energy of the PCM is related to the heat flow into and out of its chamber. Because of the assumption made that the chamber temperature is spatially uniform, this change is solely a function of time. For an internal PCM energy Q_{PCM},

$$\frac{\partial Q_{\text{PCM}}}{\partial t} = \frac{dQ_{\text{PCM}}}{dt} = -(q_{\text{teg}} + q_{\text{box}}) \tag{6.1}$$

This relationship can be leveraged to resolve the internal temperature of the PCM from an initial PCM temperature and a known exterior temperature time profile. A

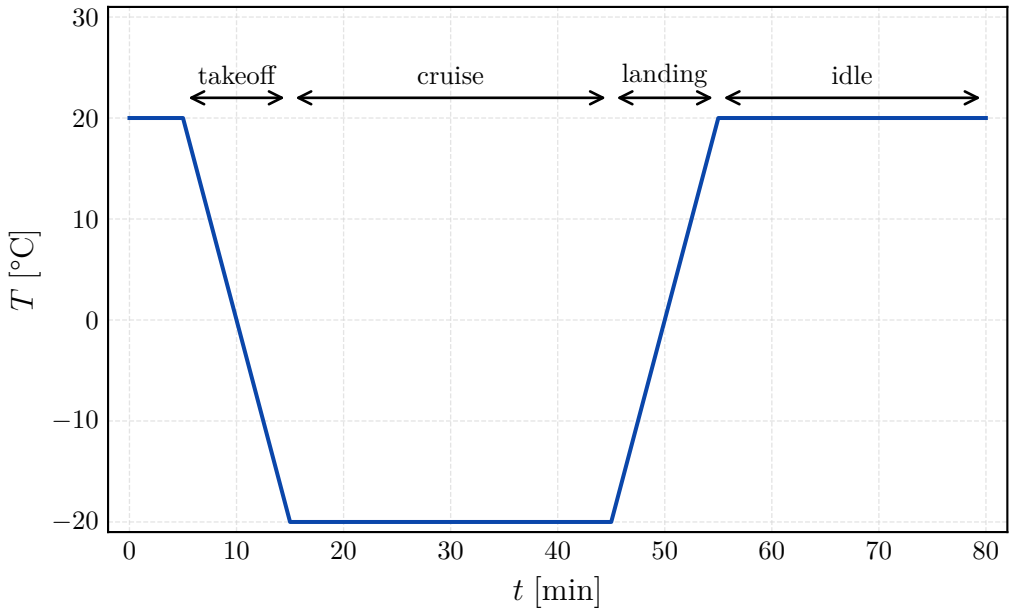

Figure 6-3: Simple flight temperature profile [22]

simple flight temperature profile for simulation is shown in Fig. 6-3. An analytical solution was found for the simple case of fixed device thermal resistance and linear exterior temperature profile [22]. However, thermoelectric systems cannot truly have a fixed thermal resistance when subjected to a variable temperature gradient because the Seebeck and Peltier effects are inherently temperature dependent. When these dependencies are included, it is difficult to solve the differential equation analytically. A simple forward-stepping discrete numerical approach can instead be used to evaluate the system. For a known state $\{T_{\text{PCM}}(t_1), T_\infty(t_1), Q_{\text{PCM}}(t_1)\}$ at time t_1, the state at time $t_1 + \Delta t$ is given by:

$$Q_{\text{PCM}}(t_1 + \Delta t) = Q_{\text{PCM}}(t_1) - \Delta t \cdot (q_{\text{teg}}(t_1) + q_{\text{box}}(t_1)) \tag{6.2}$$

$$T_{\text{PCM}}(t_1 + \Delta t) = T_{\text{PCM}}(t_1) + \frac{Q_{\text{PCM}}(t_1 + \Delta t) - Q_{\text{PCM}}(t_1)}{(mc_p)_{\text{PCM}}} \tag{6.3}$$

where $T_\infty(t_1)$ and $T_\infty(t_1 + \Delta t)$ are from the known exterior temperature profile. To forward-step this discrete model, the initial state must be known and is given as:

$$T_{\text{PCM}}(0) = T_{\text{PCM},o} \qquad T_\infty(0) = T_{\infty,o} \qquad Q_{\text{PCM}}(0) = 0 \tag{6.4}$$

Phase Change and Latent Heat

As expected, the PCM undergoes a phase change due to the exterior temperature cycle. The occurrence of a phase change during the temperature cycle is desirable because the process absorbs or releases energy without changing the temperature of the PCM. Furthermore, a fusion phase change process is desired because the low thermal conductivity of the PCM in a gaseous state would restrict heat flow to the TEG. The TEG therefore sees an improved temperature gradient and electrical output during the phase change period.

Let the latent heat of the phase change process be defined as $\mathcal{L}_{\text{PCM}}$ where the latent heat depends on the specific latent heat (of fusion) of the PCM according to

$$\mathcal{L}_{\text{PCM}} = (mL_f)_{\text{PCM}} \tag{6.5}$$

Then, during the phase change process, the change in latent heat has a similar relationship to the change in internal energy:

$$\frac{\partial \mathcal{L}_{\text{PCM}}}{\partial t} = \frac{d\mathcal{L}_{\text{PCM}}}{dt} = -(q_{\text{teg}} + q_{\text{box}}) \tag{6.6}$$

Absent supercooling, the phase change process will occur when the PCM is cooled to its phase change temperature, T_f. Again, the process can be modeled discretely by accounting for the latent heat at each time step. For an exothermic freezing process, the latent heat is initially at its maximum value of $\mathcal{L}_{\text{PCM}}$ and it decreases during the exothermic process until it reaches zero. For an endothermic melting process, the reverse occurs. For a known state $\{T_{\text{PCM}}(t_1), T_\infty(t_1), Q_{\text{PCM}}(t_1)\}$ at time t_1, the state at time $t_1 + \Delta t$ is given by:

$$\left.\begin{aligned} \mathcal{L}_{\text{PCM}}(t_1 + \Delta t) &= \mathcal{L}_{\text{PCM}}(t_1) - \Delta t \cdot (q_{\text{teg}}(t_1) + q_{\text{box}}(t_1)) \quad (6.7) \\ T_{\text{PCM}}(t_1 + \Delta t) &= T_{\text{PCM}}(t_1) \quad (6.8) \end{aligned}\right\} 0 \leq \mathcal{L}_{\text{PCM}}(t_1) \leq \mathcal{L}_{\text{PCM}}$$

The initial conditions are given at time $t_{f,o} = t(T_{\text{PCM}} = T_f)$ as:

$$\mathcal{L}_{\text{PCM}}(t_{f,o}) = \begin{cases} \mathcal{L}_{\text{PCM}} & \text{for freezing} \\ 0 & \text{for melting} \end{cases} \tag{6.9}$$
$$T_{\text{PCM}}(t_{f,o}) = T_f$$

Relationships are now defined for both sensible and latent heat changes in the device. Equations 6.2 and 6.3 describe the changes in sensible heat, and equations 6.7 and 6.3 describe the fusion phase change. The corresponding initial conditions are given in equations 6.4 and 6.9, respectively.

TEG and Insulation Heat Flow

The final task requried to resolve the model is to determine the heat flow through the insulating box and the TEG at each time point. It is straightforward to compute the flow through the insulating box with a known thermal resistance:

$$q_{\text{box}}(t) = \frac{T_{\text{PCM}}(t) - T_\infty(t)}{R_{t,\text{PCM}}} \tag{6.10}$$

To find the flow through the TEG, the models developed in Chapters 2 and 3 can be used. These models require source and sink temperature to be specified. In this case, $T_{src} = T_{\text{PCM}}$ and $T_{snk} = T_\infty$ for all time points. Because it is assumed that the PCM and its chamber are of uniform temperature, $U_{src} \to \infty$ and $T_1 \approx T_{src}$. This can be modeled in the optimization software by setting U_{src} to an arbitrarily large value.

6.2 Performance of PCM TEGs

In [22], a device design is presented and simulated for a simplified flight temperature profile using the discrete method. The simulation is re-created here using the parameters described in Table 6.1, which are considered relatively similar to those used in [22]. The heat exchange coefficient on the sink was not specified, but it was found that a value of $U = 1500\,\text{W}\,\text{m}^{-2}\,\text{K}^{-1}$ produced similar results. This is roughly

equivalent to a forced air convection around the wing of $U = 150\,\mathrm{W\,m^{-2}\,K^{-1}}$ where the heat can spread over the wing to an area ten times the TEG area. For TEGs placed sparsely throughout the wing and a plane flying reasonably fast, this heat exchanger scenario is plausible. In the simulation, the exterior temperature changes on a linear gradient from 20 °C to −20 °C and back over an 80 minute flight according to the profile given in Fig. 6-3. This temperature profile, generated energy, instantaneous power output, and instantaneous open-circuit voltage of the PCM TEG with the traditional architecture are shown in Fig. 6-4.

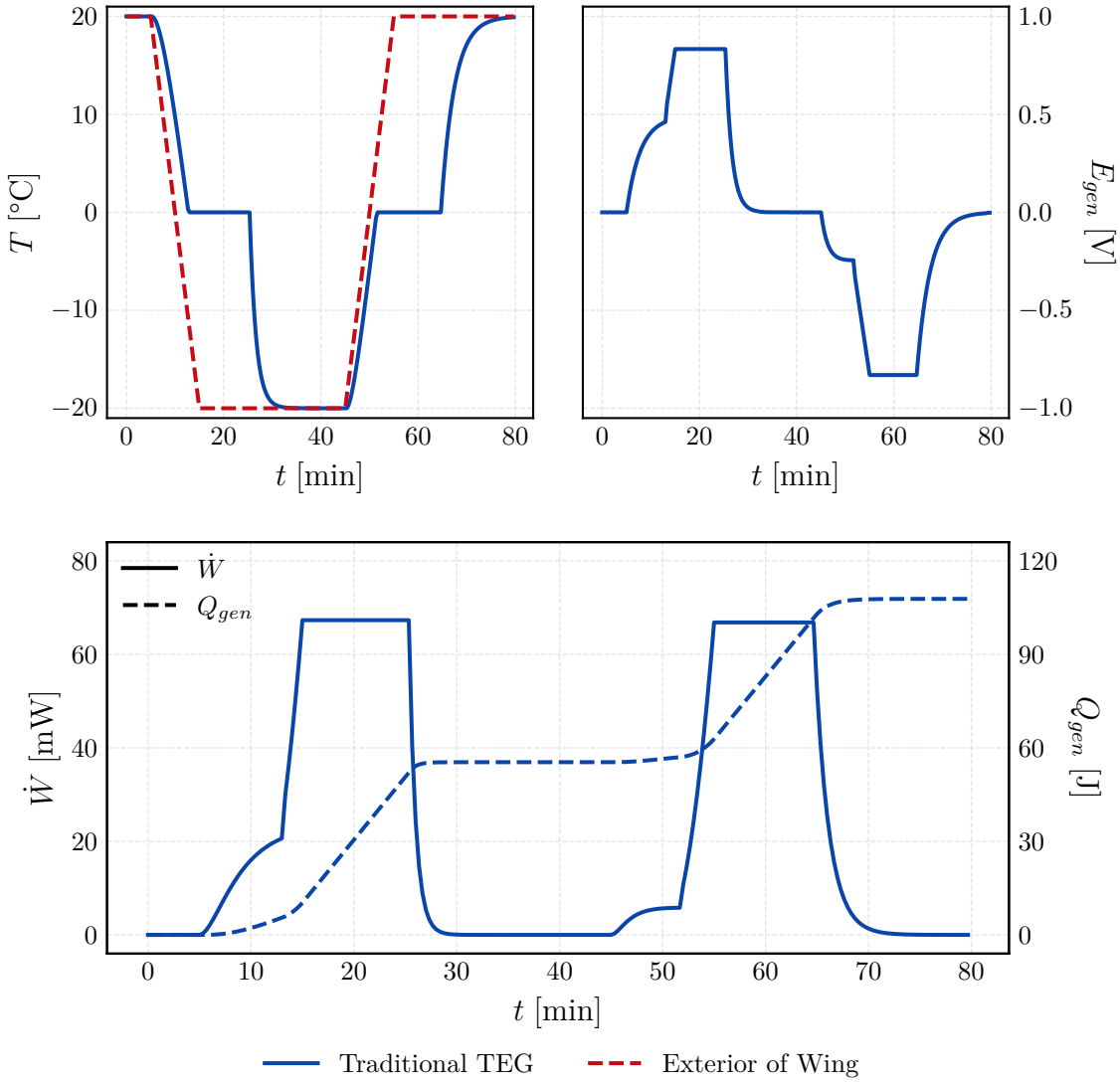

Figure 6-4: Simulated performance of traditional PCM TEG

It is evident from Fig. 6-4 that most of the energy is generated while the PCM changes phase. Ideally, then, heat transfer properties would be matched so that the PCM can fully complete a phase change as slowly as possible. It is therefore desirable for the TEG to be as thermally resistant as possible while still allowing a full phase change to occur [22]. The instantaneous power plot in Fig. 6-4 indicates that this optimum is not achieved (the same conclusion is reached in [22]). A TEG built on the distributed architecture could feasibly achieve a better thermal resistance and potentially improve energy output by de-coupling the element and device height.

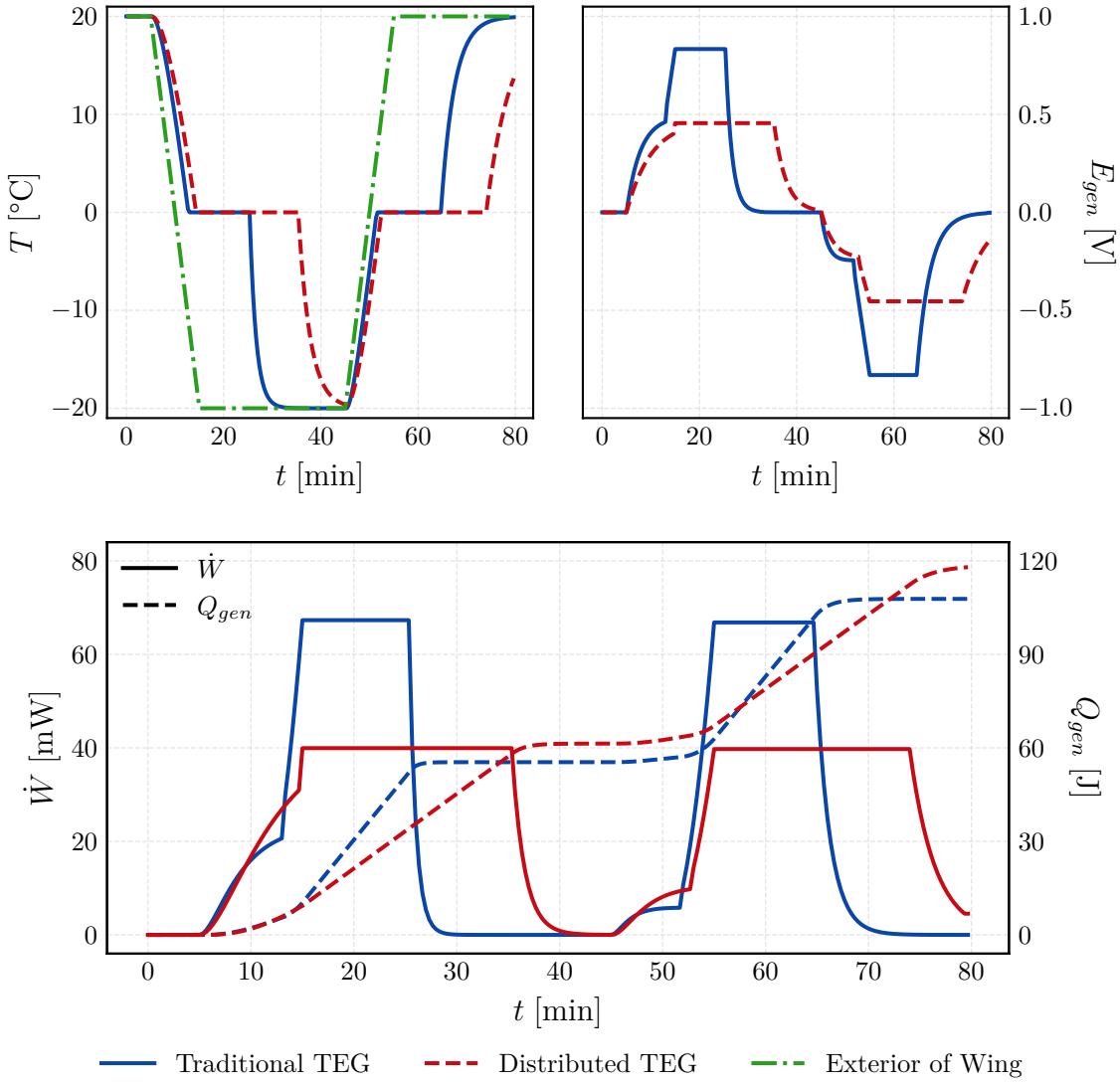

Figure 6-5: Performance comparison of traditional and distributed PCM TEGs

Simulation of a distributed TEG showed improvement over the traditional design. A single-element distributed TEG with the parameters given in Table 6.1 was simulated under the same conditions. The performance of this device is shown along with the traditional device performance in Fig. 6-5.The distributed TEG appears to nearly achieve the optimal temperature profile by reaching the minimum exterior temperature just before it begins to warm. Although the distributed TEG system produces less peak power than the traditional TEG, it generates over 9% more energy overall (118 J to 108 J) by prolonging the phase change periods. Simulation showed that a distributed TEG uses half the thermoelectric material of the traditional TEG and is twice as thick, reducing thermo-mechanical stress on the device (both the overall dimensions of the system and the dimensions of the thermoelectric elements were kept the same according to Table 6.1). This example illustrates the benefits of the expanded design space provided by the distributed architecture.

Table 6.1: Selected parameters for PCM TEG devices

Parameter	Traditional	Distributed
PCM Mass	23 g	23 g
TE Element Area	1 mm^2	1 mm^2
TE Element Height	2 mm	2 mm
Number of n-p pairs	254	127
Device Height	6.3 mm	12.6 mm
Device Area	20.25 cm	20.25 cm
U_{src}	∞	∞
U_{snk}	1500 $W\,m^{-2}\,K^{-1}$	1500 $W\,m^{-2}\,K^{-1}$

This page intentionally left blank.

Chapter 7

Conclusion and Future Work

The behavior of thermoelectric devices has been explored from an integrated perspective. Through this exploration, it was made apparent that fill factor and its effect on heat exchange can have a large effect on system performance. In the traditional thermoelectric architecture, the lower bound of fill factor is limited due to the increased thermo-mechanical stresses in this regime. Additionally, low fill factors can create a thermal short in traditional devices when the conductance of the insulator becomes greater than that of the elements. Both of these issues arise due to the coupling of the device height to the element height in the traditional architecture.

To address these issues, a novel architecture was introduced that enables integrated optimization of the thermoelectric module in conjunction with the rest of the system. The proposed distributed architecture de-couples the device and element height by connecting the elements through a series of wires rather than directly to the structural plates. The novel architecture was modeled in detail, with specific attention given to new phenomenon that must be considered (namely thermal fringing and spreading resistance). A split-element configuration was also characterized which permits segmentation of the elements in the distributed architecture.

Given the increased level of complexity associated with the distributed architecture and the desire for integrated analysis, it was determined that a programmatic solution would be most useful for modeling and optimization. A Python program was created (primarily through the GEKKO optimization package) to simulate and

optimize the distributed architecture. The program incorporates many system parameters and can be used in a variety of different ways for both generation and refrigeration applications. It was partially validated through comparison to a traditional thermoelectric device, the RC12-2.5 (II-VI Marlow, Inc.).

The program was used to simulate traditional devices and optimize distributed devices for various operating conditions. Optimal distributed devices performed equal to or better than their traditional counterparts, particularly in environments with poor heat exchange. These performance improvements were seen in both generation and refrigeration applications. Varying element dimensions further improved performance. The results clearly indicated that the introduction of new manipulable parameters through the distributed architecture and the integrated approach present new opportunities for system design.

Finally, the distributed architecture was considered in the specific application of a phase-change material generation system. Although the specified operating conditions were better suited for the traditional device and a higher fill factor, a distributed device of similar size was shown to produce 9% more power with half of the thermoelectric material.

An extensive amount of work remains: this singular introduction to integrated optimization of thermoelectric systems contrasts with the countless publications concerned with understanding the traditional architecture and relevant issues, such as cost, manufacturing, longevity, and potential applications. All such work could be expanded within the context of integrated optimization. Applications with particular potential include waste heat recovery in low temperature-gradient environments and low-power refrigeration. Additionally, prototypes and experimental work are needed to validate the modeling and assertions made here, which will in turn inform improved models and new ideas. Other topics that were given an overview here require more attention, particularly stress analysis and the specifics of segmentation in the split-element configuration. In spite of the extensive work remaining, the author hopes that this introduction of integrated design concepts and a distributed architecture contribute to the continued development of future thermoelectric systems.

Appendix A

Relevant Material Properties

Table A.1: Material properties

Material	Use	k [$\mathrm{W\,m^{-1}\,K^{-1}}$]	$\sigma \cdot 10^{-3}$ [$\Omega^{-1}\,\mathrm{m^{-1}}$]	$\rho \cdot 10^{-3}$ [$\mathrm{kg\,m^{-3}}$]	S [µV K]
N-type material[†]	n-type element	1.9	103.7	8.098	−208
P-type material[†]	p-type element	1.9	103.7	8.098	208
Extruded polystyrene [19]	Insulation	26.7×10^{-3}		56×10^{-3}	
Copper Wire	Wiring	400 [19]	58×10^{3} [41]	8.89 [41]	
Alumina silicate	Exterior Plates	30 [25]		3.97 [19][*]	
Copper Plating[‡]	Contacts	10×10^{6} [$\mathrm{W\,m^{-2}\,K^{-1}}$]	2×10^{6} [$\Omega^{-1}\,\mathrm{m^{-2}}$]		
Air [19]	Insulation	26.3×10^{-3}		1.16×10^{-3}	

[†] Deduced from RC12-2.5 data sheet [18] using method described in [30].
[‡] Estimate from II-VI Marlow, Inc.
[*] Density of alumina silicate unspecified in [25]; pure aluminum oxide substituted.

This page intentionally left blank.

Appendix B

Concept Designs

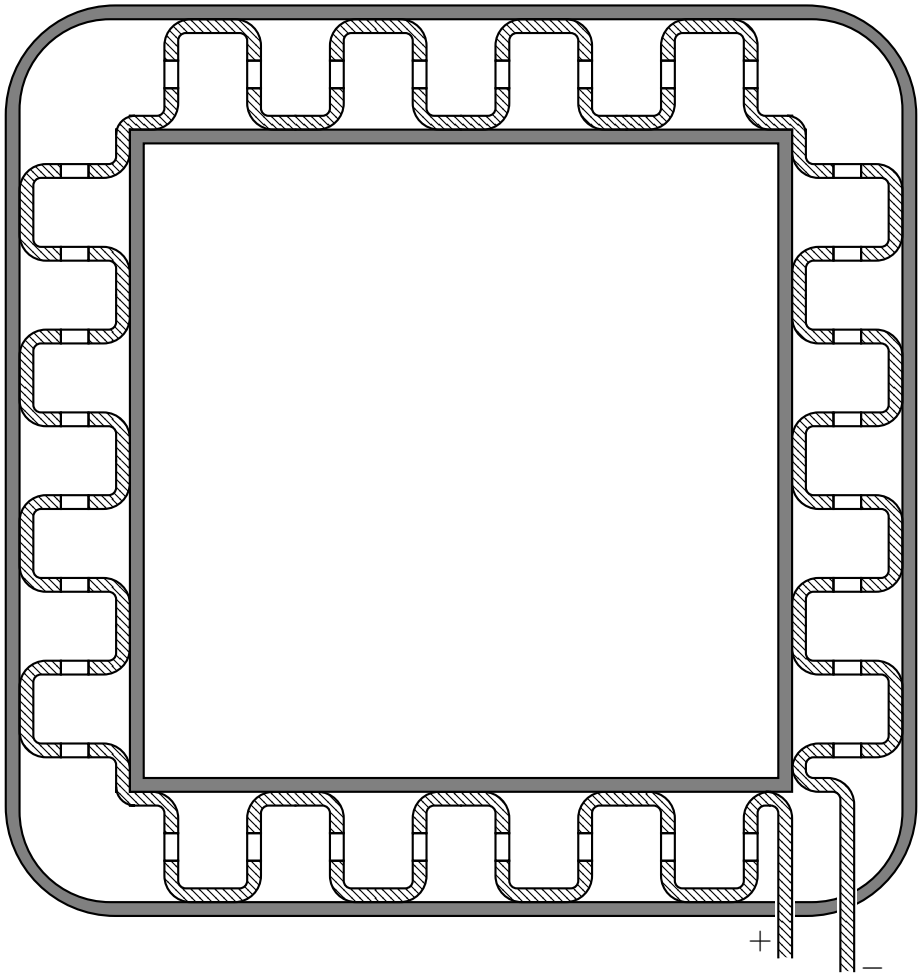

Figure B-1: Cubic distributed refrigerator concept

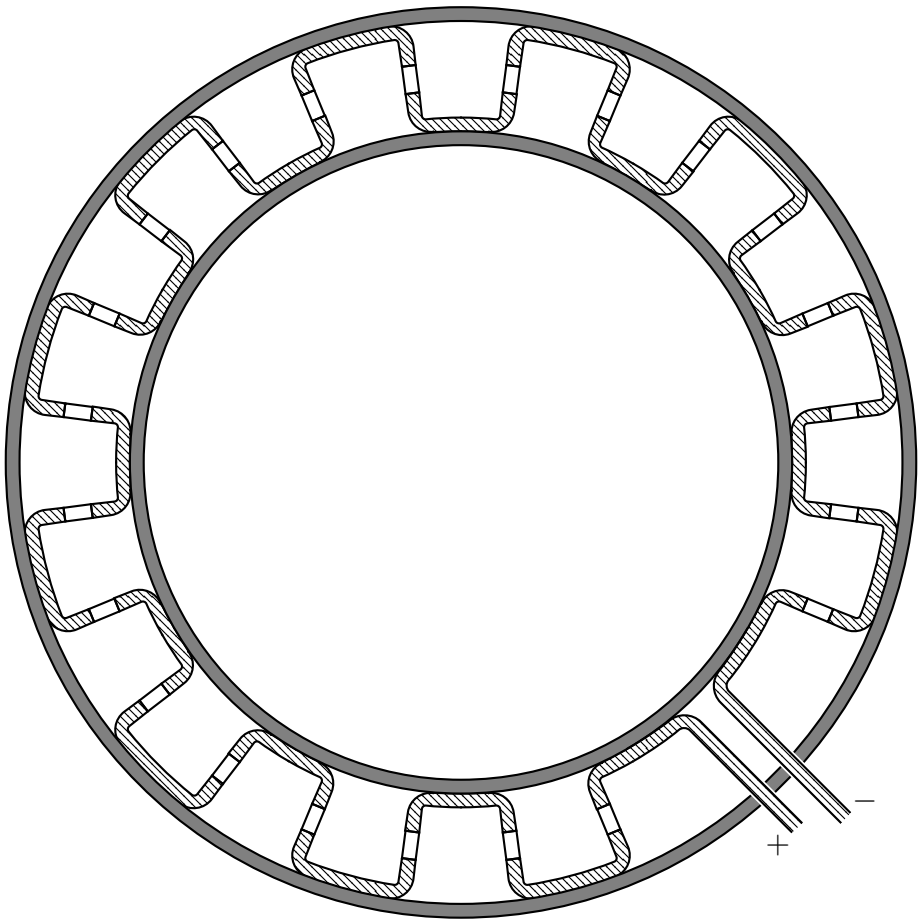

Figure B-2: Cylindrical distributed generator concept

Bibliography

[1] Elena E. Antonova and David C. Looman. Finite elements for thermoelectric device analysis in ANSYS. In *ICT 2005. 24th International Conference on Thermoelectrics, 2005.*, pages 215–218, Clemson, SC, USA, 2005. IEEE.

[2] Nicola Bailly, Jean-Marie Dilhac, Christophe Escriba, Claude Vanhecke, Nicolas Mauran, and Marise Bafleur. Energy Scavenging Based on Transient Thermal Gradients: Application to Structural Health Monitoring of Aircrafts. In *8th International Workshop onMicro and Nanotechnology for Power Generation and Energy Conversion Applications (PowerMEMS2008)*, pages 205–208, Sendai, Japan, November 2008.

[3] M. T. Barako, W. Park, A. M. Marconnet, M. Asheghi, and K. E. Goodson. Thermal Cycling, Mechanical Degradation, and the Effective Figure of Merit of a Thermoelectric Module. *Journal of Electronic Materials*, 42(3):372–381, March 2013.

[4] Logan Beal, Daniel Hill, R. Martin, and John Hedengren. GEKKO Optimization Suite. *Processes*, 6(8):106, July 2018.

[5] Lon E. Bell. Cooling, Heating, Generating Power, and Recovering Waste Heat with Thermoelectric Systems. *Science*, 321(5895):1457–1461, September 2008.

[6] Gang Chen, Yu Mu, Pengcheng Zhai, Guodong Li, and Qingjie Zhang. An Investigation on the Coupled Thermal–Mechanical–Electrical Response of Automobile Thermoelectric Materials and Devices. *Journal of Electronic Materials*, 42(7):1762–1770, July 2013.

[7] Douglas T. Crane and Gregory S. Jackson. Optimization of cross flow heat exchangers for thermoelectric waste heat recovery. *Energy Conversion and Management*, 45(9-10):1565–1582, June 2004.

[8] Jean-Marie Dilhac, Marise Bafleur, Jean-Yves Fourniols, Christophe Escriba, Robert Plana, Daniela Dragomirescu, Laurent Assouère, Patrick Pons, Hervé Aubert, and Catherine Buchheit. Cross-functional Design of Wireless Sensor Networks Applied to Aircraft Health Monitoring. In *International Workshop on Structural Health Monitoring*, pages 901–908, Stanford, CA, USA, September 2009.

[9] A. Elefsiniotis, N. Kokorakis, T. Becker, and U. Schmid. A thermoelectric-based energy harvesting module with extended operational temperature range for powering autonomous wireless sensor nodes in aircraft. *Sensors and Actuators A: Physical*, 206:159–164, February 2014.

[10] Ugur Erturun, Kaan Erermis, and Karla Mossi. Influence of leg sizing and spacing on power generation and thermal stresses of thermoelectric devices. *Applied Energy*, 159:19–27, December 2015.

[11] J. Esarte, G. Min, and D.M. Rowe. Modelling heat exchangers for thermoelectric generators. *Journal of Power Sources*, 93(1-2):72–76, February 2001.

[12] H. J. Goldsmid. *Thermoelectric Refrigeration*. Springer US, Boston, MA, 1964.

[13] H. J. Goldsmid. Conversion Efficiency and Figure-of-Merit. In *CRC Handbook of Thermoelectrics*, pages 19–25. CRC Press, Boca Raton, FL, 1995.

[14] H. Julian Goldsmid. *Introduction to Thermoelectricity*, volume 121 of *Springer Series in Materials Science*. Springer Berlin Heidelberg, Berlin, Heidelberg, 2016.

[15] Hernan E. Grecco. Pint 0.11, 2012.

[16] E. Hatzikraniotis, K. T. Zorbas, I. Samaras, Th. Kyratsi, and K. M. Paraskevopoulos. Efficiency Study of a Commercial Thermoelectric Power Generator (TEG) Under Thermal Cycling. *Journal of Electronic Materials*, 39(9):2112–2116, September 2010.

[17] J. Hedengren, J. Mojica, W. Cole, and T. Edgar. APOPT: MINLP solver for differential and algebraic systems with benchmark testing. In *INFORMS National Meeting*, volume 1417, page 47, Phoenix, AZ, USA, October 2012.

[18] II-VI Marlow, Inc. Technical Data Sheet for RC12-2.5, Single-Stage Thermoelectric Module. https://cdn2.hubspot.net/hubfs/547732/Data_Sheets/RC12-2.5.pdf.

[19] Frank P. Incropera, David P. DeWitt, Theodore L. Bergman, and Adrienne S. Lavine, editors. *Fundamentals of Heat and Mass Transfer*. John Wiley & Sons, Hoboken, NJ, seventh edition, 2011.

[20] A. F. Ioffe. *Semiconductor Thermoelements and Thermoelectric Cooling*. Infosearch, London, UK, 1957.

[21] Michail E. Kiziroglou, Dominik Samson, Thomas Becker, Steven W. Wright, and Eric M. Yeatman. Optimization of heat flow for phase change thermoelectric harvesters. In *Power MEMS 2011*, pages 454–457, Seoul, Korea, November 2011.

[22] Michail E. Kiziroglou, Steven W. Wright, Tzern T. Toh, Paul D. Mitcheson, Th. Becker, and Eric M. Yeatman. Design and Fabrication of Heat Storage Thermoelectric Harvesting Devices. *IEEE Transactions on Industrial Electronics*, 61(1):302–309, January 2014.

[23] Holger Krekel, Bruno Oliveira, Ronny Pfannschmidt, Floris Bruynooghe, Brianna Laugher, and Florian Bruhin. Pytest 5.4, 2004.

[24] Saniya LeBlanc. Thermoelectric generators: Linking material properties and systems engineering for waste heat recovery applications. *Sustainable Materials and Technologies*, 1-2:26–35, December 2014.

[25] Saniya LeBlanc, Shannon K. Yee, Matthew L. Scullin, Chris Dames, and Kenneth E. Goodson. Material and manufacturing cost considerations for thermoelectrics. *Renewable and Sustainable Energy Reviews*, 32:313–327, April 2014.

[26] R. Lougee-Heimer. The Common Optimization INterface for Operations Research: Promoting open-source software in the operations research community. *IBM Journal of Research and Development*, 47(1):57–66, 2003.

[27] Akanksha K. Menon and Shannon K. Yee. Design of a polymer thermoelectric generator using radial architecture. *Journal of Applied Physics*, 119(5):055501, February 2016.

[28] George S. Nolas, Jeffrey Sharp, and H. Julian Goldsmid. *Thermoelectrics: Basic Principles and New Materials Developments*, volume 45 of *Springer Series in MATERIALS SCIENCE*. Springer Berlin Heidelberg, Berlin, Heidelberg, 2001.

[29] Zhongliang Ouyang and Dawen Li. Modelling of segmented high-performance thermoelectric generators with effects of thermal radiation, electrical and thermal contact resistances. *Scientific Reports*, 6(1):24123, July 2016.

[30] R. Palacios, A. Arenas, R.R. Pecharromán, and F.L. Pagola. Analytical procedure to obtain internal parameters from performance curves of commercial thermoelectric modules. *Applied Thermal Engineering*, 29(17-18):3501–3505, December 2009.

[31] Herbert C Roters. *Electromagnetic Devices*. John Wiley & Sons, New York, NY, 1970.

[32] D. M. Rowe, editor. *CRC Handbook of Thermoelectrics*. CRC Press, Boca Raton, FL, 1995.

[33] D. Samson, M. Kluge, Th. Becker, and U. Schmid. Wireless sensor node powered by aircraft specific thermoelectric energy harvesting. *Sensors and Actuators A: Physical*, 172(1):240–244, December 2011.

[34] D. Samson, T. Otterpohl, M. Kluge, U. Schmid, and Th. Becker. Aircraft-Specific Thermoelectric Generator Module. *Journal of Electronic Materials*, 39(9):2092–2095, September 2010.

[35] G. Jeffrey Snyder. Application of the compatibility factor to the design of segmented and cascaded thermoelectric generators. *Applied Physics Letters*, 84(13):2436–2438, March 2004.

[36] G. Jeffrey Snyder and Eric S. Toberer. *Complex Thermoelectric Materials*, pages 101–110. Co-Published with Macmillan Publishers Ltd, UK, October 2010.

[37] G. Jeffrey Snyder and Tristan S. Ursell. Thermoelectric Efficiency and Compatibility. *Physical Review Letters*, 91(14):148301, October 2003.

[38] E. Suhir and A. Shakouri. Assembly Bonded at the Ends: Could Thinner and Longer Legs Result in a Lower Thermal Stress in a Thermoelectric Module Design? *Journal of Applied Mechanics*, 79(6):061010, November 2012.

[39] Zhiting Tian, Sangyeop Lee, and Gang Chen. A Comprehensive Review of Heat Transfer in Thermoelectric Materials and Devices. *Annual Review of Heat Transfer*, 17(N/A):425–483, 2014.

[40] S. Turenne, Th. Clin, D. Vasilevskiy, and R. A. Masut. Finite Element Thermomechanical Modeling of Large Area Thermoelectric Generators based on Bismuth Telluride Alloys. *Journal of Electronic Materials*, 39(9):1926–1933, September 2010.

[41] United States. National Bureau of Standards. *Copper Wire Tables*. Number 31 in Circular of the Bureau of Standards. Washington Government Printing Office, Washington, DC, 3rd edition, 1914.

[42] T.S. Ursell and G.J. Snyder. Compatibility of segmented thermoelectric generators. In *Twenty-First International Conference on Thermoelectrics, 2002. Proceedings ICT '02.*, pages 412–417, Long Beach, CA, USA, 2002. IEEE.

[43] S. van der Walt, S. C. Colbert, and G. Varoquaux. The NumPy array: A structure for efficient numerical computation. *Computing in Science Engineering*, 13(2):22–30, 2011.

[44] Claude Vanhecke, Laurent Assouère, Anqing Wang, Paul Durand-Estebe, Fabrice Caignet, Jean-Marie Dilhac, and Marise Bafleur. Multisource and Battery-Free Energy Harvesting Architecture for Aeronautics Applications. *IEEE Transactions on Power Electronics*, 30(6):3215–3227, June 2015.

[45] Pauli Virtanen, Ralf Gommers, Travis E. Oliphant, Matt Haberland, Tyler Reddy, David Cournapeau, Evgeni Burovski, Pearu Peterson, Warren Weckesser, Jonathan Bright, Stéfan J. van der Walt, Matthew Brett, Joshua Wilson, K. Jarrod Millman, Nikolay Mayorov, Andrew R. J. Nelson, Eric Jones, Robert Kern, Eric Larson, CJ Carey, İlhan Polat, Yu Feng, Eric W. Moore, Jake Vand erPlas, Denis Laxalde, Josef Perktold, Robert Cimrman, Ian Henriksen, E. A. Quintero, Charles R Harris, Anne M. Archibald, Antônio H. Ribeiro, Fabian Pedregosa, Paul van Mulbregt, and SciPy 1. 0 Contributors. SciPy 1.0: Fundamental algorithms for scientific computing in python. *Nature Methods*, 17:261–272, 2020.

[46] Andreas Wächter and Lorenz T. Biegler. On the implementation of an interior-point filter line-search algorithm for large-scale nonlinear programming. *Mathematical Programming*, 106(1):25–57, March 2006.

[47] Kazuaki Yazawa and Ali Shakouri. Cost-Efficiency Trade-off and the Design of Thermoelectric Power Generators. *Environmental Science & Technology*, 45(17):7548–7553, September 2011.

[48] Shannon K. Yee, Saniya LeBlanc, Kenneth E. Goodson, and Chris Dames. $ per W metrics for thermoelectric power generation: Beyond ZT. *Energy & Environmental Science*, 6(9):2561–2571, June 2013.

[49] M. M. Yovanovich, Y. S. Muzychka, and J. R. Culham. Spreading Resistance of Isoflux Rectangles and Strips on Compound Flux Channels. *Journal of Thermophysics and Heat Transfer*, 13(4):495–500, October 1999.

[50] Jianlin Yu and Hua Zhao. A numerical model for thermoelectric generator with the parallel-plate heat exchanger. *Journal of Power Sources*, 172(1):428–434, October 2007.

[51] Xiao Zhang and Li-Dong Zhao. Thermoelectric materials: Energy conversion between heat and electricity. *Journal of Materiomics*, 1(2):92–105, June 2015.

[52] Amirkoushyar Ziabari, Ephraim Suhir, and Ali Shakouri. Minimizing thermally induced interfacial shearing stress in a thermoelectric module with low fractional area coverage. *Microelectronics Journal*, 45(5):547–553, May 2014.